

3. GLOBAL OCEANS—J. M. Levy, Ed.

a. Overview—J. M. Levy

As the global ocean observing system matures and climatologies of essential climate variables grow more robust, observations of anomalous departures continue to shed light on the evolving behavior of the coupled ocean-atmosphere system. Calendar year 2009 was characterized by the following findings:

- Global SST exhibited several noteworthy features, including development of the 2009 El Niño in the tropical Pacific, transition of the Pacific Decadal Oscillation (PDO) from a two-year persistent negative phase to a positive phase during the fall/winter 2009, substantial cooling in the mid-latitude North Atlantic from May 2009 to December 2009, and significant warming in the tropical Indian Ocean from influences of the 2009 El Niño.
- During the latest El Niño a considerable build up of heat was observed in the upper equatorial Pacific Ocean. Global integrals of upper-ocean heat content for the last several years have reached values consistently higher than for all prior times in the record, demonstrating the dominant role of the oceans in the Earth's energy budget.
- Ocean heat fluxes played a dual role in the dynamics of large-scale SST anomalies. Heat fluxes generated SST anomalies in some regions (such as in the North Atlantic and the tropical Indian Oceans) while acting to dampen SST anomalies that had already been generated in other regions (such as in the tropical and extratropical Pacific).
- The surface of the western equatorial Pacific freshened considerably from 2008 to 2009, at least partially owing to an eastward spreading of the western equatorial fresh pool along the equator during this latest El Niño. Outside the more variable tropics, the anomalously salty surface values of salinity in climatologically drier locations and anomalously fresh values in rainier locations observed since 2004 generally persisted into 2009, suggesting an increase in the hydrological cycle consistent with climate model predictions for global warming scenarios.
- Very strong eastward surface current anomalies were seen across the equatorial Pacific,

associated with the El Niño event of 2009. Such current anomalies typically lead eastern Pacific SST anomalies by several months. By the last two months of 2009, the anomalies had reached values similar to the 2002 El Niño, exceeded during the altimetry age (1993–present) only by the 1997/98 El Niño.

- Unusually low Florida Current transports were observed in May and June of 2009, a time of year that transport is typically high. This low-transport event was linked to unusually high sea level and coastal flooding along the east coast of the United States in the summer of 2009.
- Sea level variations during 2009 were strongly affected by the transition from La Niña to El Niño conditions, especially in the tropical Indo-Pacific. Globally, variations about the long-term trend also appear to have been influenced by ENSO, with a slight reduction in global mean sea level during the 2007/08 La Niña event, and a return to the long-term trend and perhaps slightly higher values during the latter part of 2009 and the current El Niño event.
- The global ocean CO₂ uptake flux for 2008, the most recent year for which analyzed data are available, is estimated to have been 1.23 Pg C yr⁻¹, which is 0.25 Pg C yr⁻¹ smaller than the long-term average. This lower uptake is significant when compared to the 1σ interannual variability estimate of ±0.14 Pg C yr⁻¹ for the whole 27-year record. The total global ocean inventory of anthropogenic carbon stored in the ocean interior as of 2008 is 151 Pg C. This estimate suggests a 33 Pg C increase in inventory since 1994, reflecting uptake and storage of anthropogenic CO₂ at rates of 2.0 and 2.3 ±0.6 Pg C yr⁻¹ for the decades of the 1990s and 2000s, respectively.
- The downward trend in global chlorophyll observed since 1999 has continued through 2009, with current chlorophyll stocks in the central stratified oceans now approaching record lows since 1997.

b. Sea surface temperatures—Y. Xue, R. W. Reynolds, and V. Banzon

The unique features in the global SST in 2009 include (1) the development of the 2009/10 El Niño in the tropical Pacific, (2) the transition of the PDO from a 2-year persistent negative phase to a positive phase during the fall/winter 2009, (3) a significant warming in the tropical Indian Ocean, and (4) a substantial cooling in the mid-latitude North Atlan-

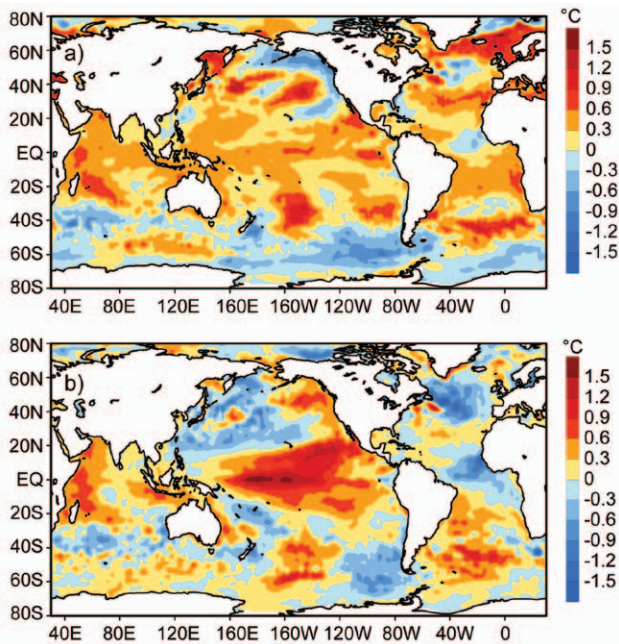


FIG. 3.1. (a) Yearly mean SSTAs in 2009 and (b) SSTA differences between 2009 and 2008. SSTs are the monthly fields interpolated from the weekly 1° OISST of Reynolds et al. (2002). All anomalies are defined as departures from the 1971–2000 climatology (Xue et al. 2003).

tic. We used the Optimal Interpolation SST version 2 (OISST v.2), which is a weekly analysis on a one-degree grid derived by combining in situ and satellite observations for the period of November 1981 to present (Reynolds et al. 2002). To put the 2009 SST in a historical perspective, we also analyzed the Extended Reconstructed SST version 3b (ERSST.v3b), which is a monthly merged land-ocean surface temperature analysis on a two-degree grid for the period of 1854 to present (Smith et al. 2008). SST anomalies (SSTA) are defined as departures from the 1971 to 2000 climatology described by Xue et al. (2003).

The yearly mean SSTA in 2009 is characterized by overall positive SSTA in all the tropical oceans, and negative SSTA south of 40°S. The 2009 SSTA has a negative PDO pattern in the North Pacific, and a tripole pattern in the North Atlantic (Fig. 3.1a). The 2009 minus 2008 SSTA differences show signatures of the development of the 2009/10 El Niño and the transition of the PDO from a negative to positive

phase (Fig. 3.1b). It also indicates a substantial warming in the tropical Indian Ocean and a cooling in the equatorial Atlantic and the mid-latitude North Atlantic.

The 2009/10 El Niño was preceded by weak La Niña conditions during the winter 2008/09 (Fig. 3.2a). The tropical Pacific returned to near-normal conditions during boreal spring (Fig. 3.2b), and transitioned into weak El Niño conditions (Niño3.4 > 0.5°C) during boreal summer (Fig. 3.2c). The June–July–August seasonal mean SSTA was about +1.2°C in the far eastern equatorial Pacific. It is noteworthy that there were two additional SSTA maxima of about +0.9°C, one in the subtropical northwestern Pacific that might be related to the positive SSTA in the central North Pacific, and another one in the northeastern Pacific near the coast of Mexico. The positive SSTA in the central-eastern equatorial Pacific strengthened rapidly in October–November 2009, and the 3-month-running mean Niño3.4 (170°W–120°W, 5°N–5°S) SST was about 1°C above-normal in September–November 2009, indicating a moderate strength of El Niño (Fig. 3.2d). At the same time, the positive SSTA in the subtropical northwestern Pacific weakened rapidly. It is interesting to note that the positive SSTA in the northeastern tropical Pacific persisted while that in the southeastern tropical Pacific dissipated quickly and switched into negative SSTA in boreal fall. The El Niño reached a peak phase during December 2009, and the SSTA pattern in January 2010 falls into the category of the central-Pacific event or Modoki event (Ashok et al. 2007) in which the larg-

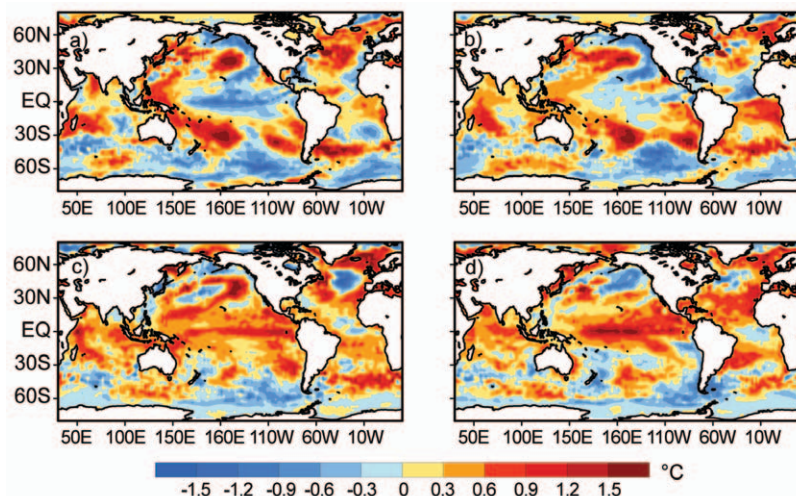


FIG. 3.2. Seasonal mean SSTAs (°C) for (a) December 2008 to February 2009, (b) March to May 2009, (c) June to August 2009 and (d) September to November 2009. SSTs are the monthly fields interpolated from the weekly 1° OISST of Reynolds et al. (2002). All anomalies are defined as departures from the 1971–2000 climatology (Xue et al. 2003).

est warming is centered near the date line. Since June 2009 there have been four episodes of downwelling oceanic Kelvin waves associated with westerly wind burst events, which are believed to contribute to the maintenance and strengthening of the 2009/10 El Niño (see “Monthly Ocean Briefing” slides from the Climate Prediction Center (CPC), NCEP, at <http://www.cpc.ncep.noaa.gov/products/GODAS>).

The SSTA in the North Pacific was dominated by a negative PDO pattern during the winter 2008/09 and spring 2009, characterized by a horseshoe pattern of positive SSTA extending from the equatorial western Pacific to the mid-latitudes in both hemispheres and negative SSTA extending along the west coast of North America (Fig. 3.2a and Fig. 3.2b). Consistent with the negative PDO phase, upwelling along the west coast of North America was mostly above-normal during the winter 2008/09 and spring 2009 (see the CPC “Monthly Ocean Briefing” referred to above). During summer 2009, the PDO phase returned to near-normal (see the PDO index at <http://jisao.washington.edu/pdo>, Mantua et al. 1997) and El Niño conditions developed in the tropical Pacific (Fig. 3.2c). During fall 2009, the El Niño conditions intensified, while the PDO phase remained near-normal. Note that the PDO phase became weakly above-normal in January 2010, indicating that atmospheric teleconnections from the El Niño started to influence SST in North Pacific.

The tropical Indian Ocean SSTA increased substantially from 2008 to 2009. Figure 3.1a shows that the yearly mean SSTA in 2009 was about $+0.3^{\circ}\text{C}$ ($+0.6^{\circ}\text{C}$) in the central-eastern (western and southwestern) tropical Indian Ocean. The 2009 minus 2008 SSTA differences indicate that SSTA increased by more than 0.6°C in the western and south-eastern tropical Indian Ocean (Fig. 3.1b). As a result, 2009 became the second warmest year in the tropical Indian Ocean behind 1998 when the record warming occurred, which is seen from the basin mean yearly SSTA indices derived from ERSST.v3b for 1950–2009 (Fig. 3.3b). The increase in the tropical Indian Ocean SST is clearly associated with that in the tropical Pacific Ocean SST (Fig.

3.3c). The section in this chapter on “Global Ocean Heat Fluxes” (Yu and Weller 2007), suggests that the basin-wide warming in the tropical Indian Ocean from July to December 2009 can be largely attributed to decrease of latent and sensible heat fluxes due to weakened trade winds from influences of the 2009 El Niño. Figure 3.3c also suggests that the tropical Indian Ocean SST usually warms up significantly in the years following El Niño, e.g., in 1998, 1987, and 1983. The warming in 2009 is somewhat unusual in the sense that it occurred during the El Niño year, rather than in the year after El Niño.

The historical perspective of the 2009 SSTA has been shown separately for the (a) global ocean, (b) tropical Indian, (c) tropical Pacific, (d) North Pacific, (e) tropical Atlantic, and (f) North Atlantic in Fig. 3.3. For the global ocean, the SSTA increased from 0.15°C in 2008 to 0.25°C in 2009, and became the fourth warmest year behind 1998, 2003, and 2005, the top three warmest years since 1950 (Fig. 3.3a). The five year running mean of the yearly-mean time series of global SSTA shows that SSTs have trended downward since 2003. However, the downward trend is punctuated by the two consecutive La Niñas in 2007 and 2008, which lowered the global mean SST. For the tropical Pacific, the SSTA increased from 0.08°C in 2008 to 0.34°C in 2009, and also became the fourth warmest year behind 1997, 2004, and 2002 since 1950

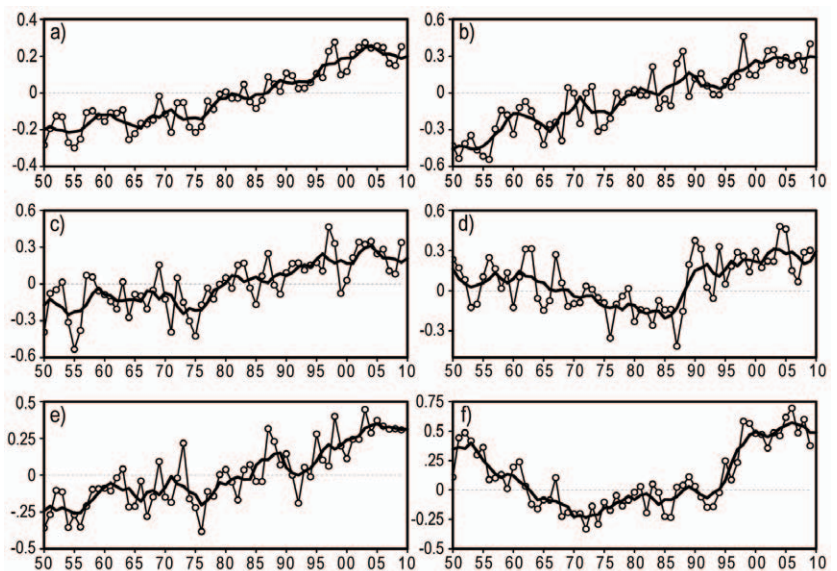


FIG. 3.3. Yearly mean SSTAs ($^{\circ}\text{C}$) (dots) averaged in the (a) global ocean, (b) tropical Indian (30°S – 30°N), (c) tropical Pacific (30°S – 30°N), (d) North Pacific (120°E – 110°W , 30°N – 60°N), (e) tropical Atlantic (30°S – 30°N), (f) North Atlantic (80°W – 0° , 30°N – 60°N) in 1950–2009. Black lines are the five-year running means of the yearly mean SSTAs. SSTs are the Extended Reconstructed SST version 3b of Smith et al. (2008). All anomalies are defined as departures from the 1971–2000 climatology (Xue et al. 2003).

(Fig. 3.3c). It is interesting that the tropical Atlantic SSTA peaked in 2003 and has decreased slowly since then (Fig. 3.3e). The North Pacific SST changed little from 2008 to 2009 and has been persistently above-normal since 1990 (Fig. 3.3d). The North Atlantic SSTA decreased from 0.6°C in 2008 to 0.38°C in 2009 and became the coolest year since 2002 (Fig. 3.3f).

The substantial cooling in the mid-latitude North Atlantic in 2009 is further analyzed here. In Fig. 3.4, we show the evolution of the zonal average SSTA in the North Atlantic along with the CPC North Atlantic Oscillation index and the zonal average LHF+SHF (latent and sensible heat flux) anomalies based on the Objectively Analyzed air-sea Fluxes (OAFlux)

project during November 2008–December 2009 (Yu and Weller 2007; <http://oaflex.whoi.edu>). During the early winter 2008/09, positive SSTA of about +1.5°C were present in the North Atlantic at 40°N–50°N, and SSTA of about +0.6°C in the tropical North Atlantic (TNA, hereafter) at 5°N–15°N. The two maxima of positive SSTA suddenly weakened during January 2009, which coincided with the sudden increase of LHF+SHF at 40°N–60°N and 0°–20°N. The positive LHF+SHF anomalies in the TNA persisted from January 2009 into February 2009, while those in middle-high latitudes propagated southward into the subtropics, contributing to the SST cooling in the TNA in February 2009. The middle-latitude SST further decreased and became negative in May 2009, probably forced by the positive LHF+SHF anomalies in April–May 2009. The three subsequent cooling episodes of SST that occurred during September, November, and December 2009 correspond well with the three maxima of positive LHF+SHF anomalies. The persistence of the negative SSTA from May 2009 to January 2010 can probably be attributed to the negative North Atlantic Oscillation (NAO) phases during June, July, October, and December 2009, which often cool the SST in middle latitudes and warm the SST in high latitudes and subtropics (Deser and Blackmon 1993), referred to as a negative SST dipole pattern here. The coincidence between negative NAO phases and negative SST dipole patterns seems to support the hypothesis that air-sea coupling plays a significant role in the seasonal variability of the NAO and North Atlantic SST (Czaja and Frankignoul 2002). It is also noted that the positive SSTA persisted and shifted southward, which is also consistent with the tripole SST pattern forced by the NAO. Therefore, the development of the positive SSTA in the TNA during summer can probably be attributed to the strong negative NAO during summer and the subsequent maintenance and enhancement of the TNA SST during fall/winter is likely due to the negative NAO during fall/winter.

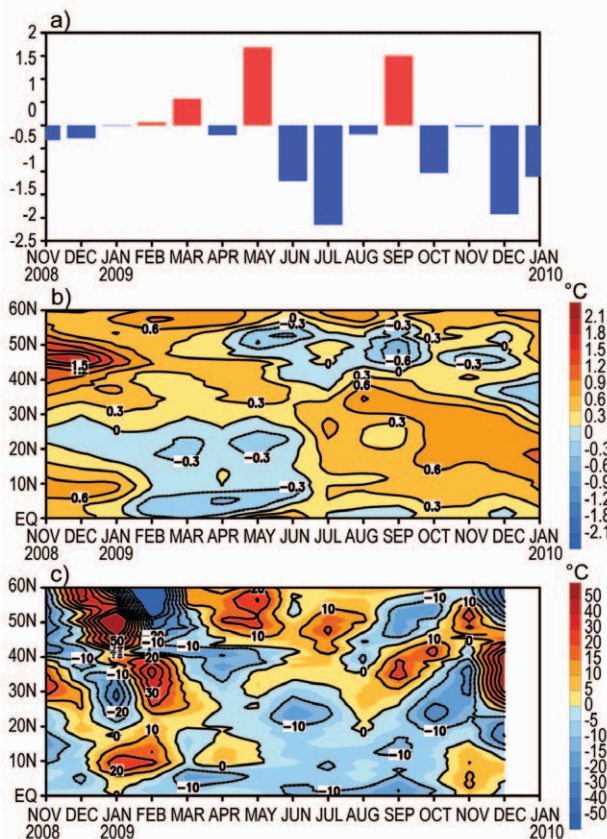


FIG. 3.4. (a) Monthly standardized NAO index derived from monthly standardized 500-mb height anomalies obtained from the NCEP CDAS in 20°N–90°N (<http://www.cpc.ncep.noaa.gov>). Time–latitude sections of (b) SSTA and (c) LHF+SHF (latent and sensible heat flux) anomalies (upward positive) averaged between 80°W and 20°W. SSTs are the monthly fields interpolated from the weekly 1° OISST of Reynolds et al. (2002), and anomalies are defined as departures from the 1971–2000 climatology (Xue et al., 2003). LHF+SHF are the Objectively Analyzed air–sea Fluxes (OAFlux) (Yu and Weller 2007), and anomalies are defined as departures from the 1988–2008 climatology (personal communication with Dr. Lisan Yu).

c. *Ocean heat content*—G. C. Johnson, J. M. Lyman, J. K. Willis, S. Levitus, T. Boyer, J. Antonov, M. D. Palmer, and S. A. Good

Storage and transport of heat in the ocean are central to aspects of climate such as El Niño (Zebiak 1989), the North Atlantic Oscillation (Curry and McCartney 2001), hurricanes (Mainelli et al. 2008), sea level rise (Domingues et al. 2008), the global energy budget (Trenberth 2009), and constraining global warming scenarios (Knutti and Tomassini 2008). The accompanying sidebar gives additional perspective.

We begin by discussing an estimate of upper-ocean (0–750 m) heat content anomaly (OHCA) for the period 1 January–31 December 2009 (Fig. 3.5a) computed from a combination of in situ ocean temperature data (World Ocean Database 2009 – Johnson et al. 2009a and Argo – Roemmich et al. 2009) and satellite altimetry data following Willis et al. (2004) but relative to a 1993–2009 baseline (the altimetry time period), hereafter the combined estimate. We also discuss changes in the combined estimate between 2009 and 2008 (Fig. 3.5b), as well as maps of the linear trend of the combined estimate from 1993–2009 and its statistical significance (Fig. 3.6). Finally, we present three different time series of global integrals of in situ only estimates of upper OHCA (Fig. 3.7).

In recent years many of the globally distributed in situ subsurface ocean temperature data are from Argo. Data from Argo floats with the potential for as yet uncorrected systematic pressure biases (http://www.argo.ucsd.edu/Acpres_drift_apex.html) have been removed from the combined estimate. In ad-

dition, annual estimates of XBT fall rate corrections have been applied for deep and shallow probe data using Table 2 of Wijffels et al. (2008) but with no XBT data used after 2005. Details of all the fields analyzed here may change after more Argo real-time data are subject to delayed-mode scientific quality control, as more data are reported, and as XBT and MBT corrections improve.

The combined estimate of OHCA in 2009 (Fig. 3.5a) shows eddy and meander variability down to the 100-km mapping scales, as does, to a greater extent, the difference of the 2009 and 2008 combined estimates (Fig. 3.5b). Strong small-scale spatial variability in OHCA fields is associated with the western boundary currents in every gyre, as well as the Antarctic Circumpolar Current (Fig. 3.5b). The difference in the combined estimates between 2009 and 2008 (Fig. 3.5b) illustrates the large year-to-year variability in ocean heat storage. Of course internal ocean dynamics, such as advection and heave, certainly play a significant role in many of these changes but for purposes of comparison only, they reach or exceed the equivalent of a 95 W m^{-2} magnitude surface flux applied over one year ($\sim 3 \times 10^9 \text{ J m}^{-2}$). Upper OHCA, deep variability, freshwater, and mass signals all contribute to sea level anomalies. Despite this, there are many large-scale visual similarities between the combined estimate (Fig. 3.5a) and sea level (Fig. 3.22 top) fields in 2009, even relative to their differing baseline periods. This similarity shows the large contribution of heat content variations to sea level variations.

Large-scale patterns are evident in the combined estimate of OHCA for 2009 (Fig. 3.5a) and its difference from 2008 (Fig. 3.5b). The equatorial Pacific gained heat during the El Niño that commenced this year (see also Fig. 4.7) as did the off-equatorial central and eastern tropical Pacific. Despite declines in OHCA in the western tropical Pacific (excepting the Coral Sea that gained heat since 2008), OHCA there remains well above the mean. While the annual averaging period presented here is too long for detailed study of the ocean advection of heat associated with ENSO dynamics (but see Chapter 4), certainly those processes contribute to the change on the equator and perhaps those in the off-equatorial regions (Zebiak 1989).

The North Pacific shows high OHCA in its center in 2009, with low OHCA to the south, off the west coast of North America and into the eastern Bering Sea (Fig. 3.5a). This pattern is consonant with a negative Pacific Decadal Oscillation index (Mantua et al.

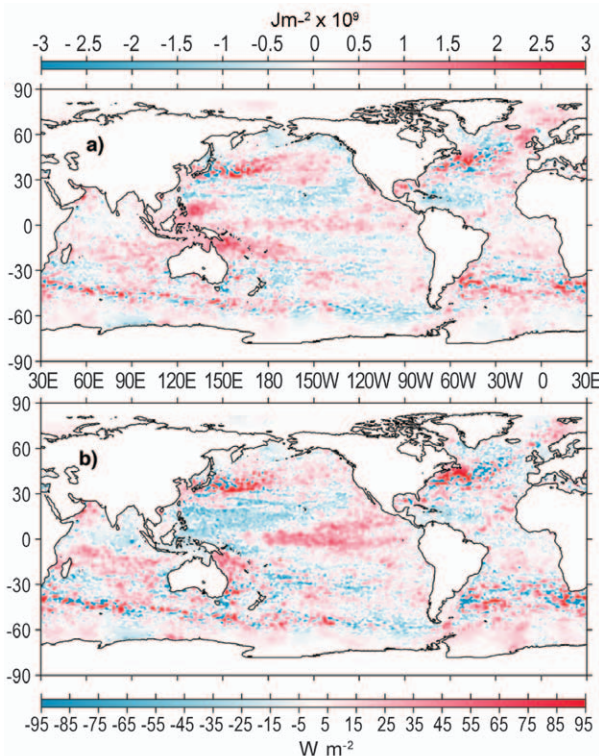


FIG. 3.5. (a) Combined satellite altimeter and in situ ocean temperature data estimate of upper (0–750 m) ocean heat content anomaly OHCA (10^9 J m^{-2}) for 2009 analyzed following Willis et al. (2004), but relative to a 1993–2009 baseline. (b) The difference of 2009 and 2008 combined estimates of OHCA expressed as a local surface heat flux equivalent (W m^{-2}). For panel comparisons, note that 95 W m^{-2} applied over one year results in a $3 \times 10^9 \text{ J m}^{-2}$ change of OHCA.

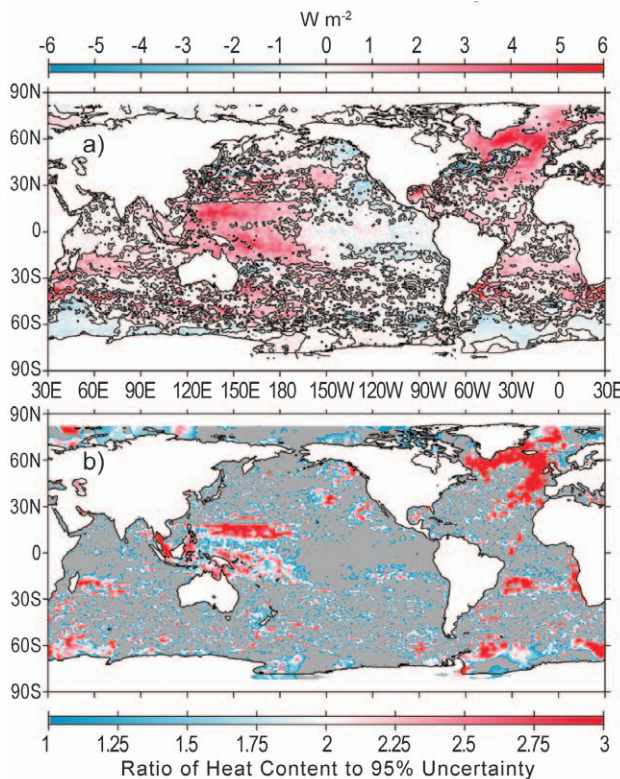


FIG. 3.6. (a) Linear trend from 1993 to 2009 of the combined satellite altimeter and in situ ocean temperature data estimate of upper (0–750 m) ocean heat content anomaly OHCA (W m^{-2}) analyzed following Willis et al. (2004). (b) Ratio of the linear trend to its 95% uncertainty estimate, with colored areas showing regions with statistically significant trends, and grey areas those without.

1997) from late 2007 through mid 2009. The band of high OHCA along 35–50°S in the South Pacific (Fig. 3.5a) appears to have steadily migrated south from tropical latitudes since 2006 (Arguez 2007; Levinson and Lawrimore 2008; Peterson and Baringer 2009).

The Indian Ocean is mostly warmer than the baseline in 2009 (Fig. 3.5a). The northern Arabian Sea and the Indian Ocean west of the Indonesian Seas gained heat between 2008 and 2009 (Fig. 3.5b) and stand out as warmer than the rest of the region in 2009.

In the Subpolar North Atlantic, the Labrador and Irminger Seas, which cooled between 2007 and 2008 (Peterson and Baringer 2009) continued to cool between 2008 and 2009 (Fig. 3.5b), so OHCA values in these areas are now below the 1993–2009 mean (Fig. 3.5a). This change is consonant with a return of deep wintertime convection in this region during early 2008 (Våge et al. 2009) and the associated export of heat from ocean to atmosphere. The continued high OHCA values in the eastern subpolar North Atlantic (Fig. 3.5a) suggest that subtropical influences are still

strong there, consistent with anomalously salty surface conditions in that region in 2009 (Fig. 3.13a). The subtropical and tropical Atlantic in both hemispheres remains slightly warmer than the mean, with little change from 2008 to 2009.

Near the Antarctic Circumpolar Current, OHCA is highly variable (Fig. 3.5a), but appears anomalously warm around the globe, consistent with recent studies (Böning et al. 2008), except perhaps in the eastern Pacific. Western boundary current extensions in the North Pacific and both hemispheres of the Atlantic are energetic, with large year-to-year changes (Fig. 3.5b).

A few very distinct (Fig. 3.6a) and statistically significant (Fig. 3.6b) regional patterns in the Pacific

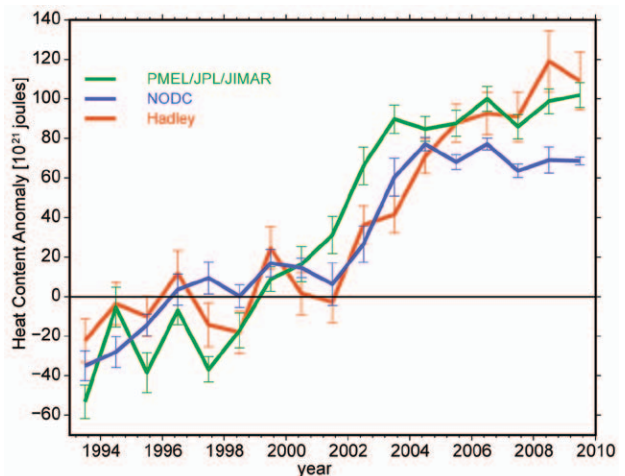


FIG. 3.7. Time series of annual average global integrals of in situ estimates of upper (0–700 m) OHCA (10^{21} J, or ZJ) for 1993–2009 with standard errors of the mean. Error estimates displayed do not contain uncertainties due to differences in climatology, treatment of the seasonal cycle, mapping methods, instrument bias corrections, or quality control. The NODC estimate follows Levitus et al. (2009). The PMEL/JIMAR estimate is a weighted integral with sampling errors (Lyman and Johnson 2008) using Argo and WOD 2009 (Johnson et al. 2009a) data relative to a 1993–2002 climatology with the Wijffels et al. (2008) Table 2 XBT bias adjustments applied and no XBT data after 2005. The Hadley estimate applies XBT bias adjustments from Table 1 of Wijffels et al. (2008) to the EN3 dataset (Ingleby and Huddleston 2007; www.metoffice.gov.uk/hadobs) relative to a 1993–2002 climatology and is computed from estimates of monthly OHCA following Palmer et al. (2007) and Palmer and Brohan (2010, manuscript submitted to *Int. J. Climatol.*) with error estimate methodology similar to Rayner et al. (2006) but adding uncertainty in the XBT bias correction. For comparison, the NODC estimate has been offset relative to its 1993–2002 mean, the climatology time period for the other estimates.

and Atlantic Ocean stand out in the 1993–2009 local linear trends of OHCA. In the Atlantic Ocean, the Labrador, Irminger, and Greenland-Iceland-Norwegian Seas have all trended warmer over the interval, reflecting a robust regional warming trend over the longer time period (Fig. 3.6a) that has not been overcome by the recent cooling there (Fig. 3.5a) in the last few years. These changes are related to variations in the NAO index. In addition, the eastern portions of the Atlantic trended warmer across both hemispheres. As in the 2009 OHCA map, areas of warming appear more widespread than areas of cooling.

The statistically significant (Fig. 3.6b) 1993–2009 regional trends in the Pacific Ocean (Fig. 3.6a) are of warming in the western tropical Pacific and off-equatorial cooling in the east, consistent with general strengthening of the subtropical-tropical circulation in the past two decades (McPhaden and Zhang 2004). The statistically significant warming in the central North Pacific and cooling south of Alaska and off the west coast of North America are also consistent with an overall downward trend in the PDO index (Mantua et al. 1997) from 1993 to 2009.

Three different upper ocean estimates (0–700 m) of globally integrated in situ OHCA (Fig. 3.7) reveal a large increase in global integrals of that quantity since 1993. The interannual details of the time series differ for a variety of reasons including differences

in climatology, treatment of the seasonal cycle, mapping methods, instrument bias corrections, quality control, and other factors. Most of these factors are not taken into account in the displayed uncertainties, so while the error bars shown do not always overlap among the three estimates, these estimates are not necessarily statistically different from each other because the error bars are likely unrealistically small. Even so, errors are too large to obtain reliable trends over a few years. However, the three curves all agree on a significant decadal warming of the upper ocean since 1993, accounting for a large portion of the global energy imbalance over this time period (Trenberth 2009), and the three sets of maps (not shown) from which the curves are produced show similar large-scale features.

d. Global ocean heat fluxes—L. Yu and R. A. Weller

Most of incoming solar energy absorbed by Earth is absorbed at the top ocean layer, but not all the absorbed heat is stored and transported by the oceans. Over 80% of the heat is released back to the atmosphere by two heat exchange processes at the air-sea interface: evaporation that releases latent heat and conduction, and convection that releases sensible heat. The amount of heat being exchanged is called heat flux. Latent and sensible heat fluxes from the oceans are significant energy sources for global atmo-

RECENT ADVANCES IN OUR UNDERSTANDING OF GLOBAL OCEAN HEAT CONTENT—M. D. PALMER, K. HAINES AND J. M. LYMAN

Quantifying and understanding changes in global and regional ocean heat content (OHC) are of fundamental importance to climate science. The long-term increase in OHC has an important contribution to sea level rise (Antonov et al. 2002, 2005; Domingues et al. 2008), reflects a first-order estimate of Earth's radiation balance (Levitus et al. 2005; Murphy et al. 2009), and provides a powerful constraint on model projections of future surface temperature rise (Knutti and Tomassini 2008). Here we review some of the major progress made in OHC research since publication of the IPCC Fourth Assessment Report (AR4) (Fig. 3.8).

The first major advance is the quantification of a time-varying warm bias in the expendable bathythermograph data (XBT), which constitute a large fraction of the historical subsurface temperature observations (Gouretski and Koltermann 2007). This warm bias, in combination with a small number of faulty Argo floats, was responsible for the spurious cooling seen in the AR4 results over the period 2003–05 (Fig. 3.8; Willis et al. 2007). We note that since profiling floats are still a relatively new technology, there may

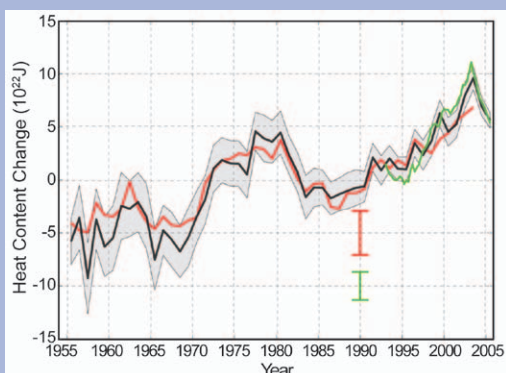


FIG. 3.8. The IPCC AR4 estimates of annual ocean heat content anomaly (10^{22} J) for the 0–700 m layer. The black curve is updated from Levitus et al. (2005), with the shading representing the 90% confidence interval. The red and green curves are updates of the analyses by Ishii et al. (2006) and Willis et al. (2004, over 0–750 m) respectively, with the error bars denoting the 90% confidence interval. Anomalies are computed relative to the 1961–90 average. Figure reproduced from Bindoff et al. (2007).

Continues on next page

cont' RECENT ADVANCES IN OUR UNDERSTANDING OF GLOBAL OCEAN HEAT CONTENT—M. D. PALMER, K. HAINES AND J. M. LYMAN

be some unresolved biases in the Argo data. Several groups have estimated XBT bias corrections and computed OHC time-series – a marked increase in OHC work since the AR4. These new XBT-corrected OHC time series (Fig. 3.9) show a reduction in the decadal variability compared to the AR4 results (Fig. 3.8), improving agreement with coupled climate model simulations (Domingues et al. 2008). However, there are still considerable differences in interannual variability among the XBT-corrected curves that require further investigation. The impact of XBT corrections on the long-term trend varies (Wijffels et al. 2008; Ishii and Kimoto 2009; Levitus et al. 2009; Gouretski and Reseghetti 2010), but all the time series show an underlying rise in OHC consistent with our understanding of anthropogenic climate change.

The limited historical ocean sampling (AchutaRao et al. 2006) has motivated a novel approach to understanding the observed changes in OHC from a more mechanistic point of view. Palmer et al. (2007) have evaluated the ocean warming signal relative to fixed isotherms. This approach seeks to separate the influence of air-sea heat flux and ocean circulation in observed OHC change by measuring the average temperature above an isotherm and isotherm depth, respectively (Palmer and Haines 2009).

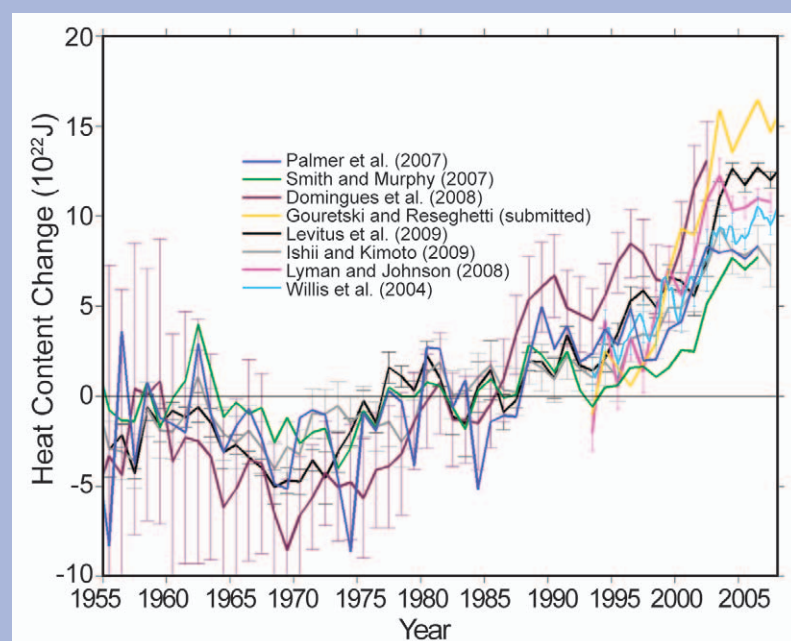


FIG. 3.9. XBT corrected estimates of annual ocean heat content anomaly (10^{22} J) for the 0–700 m layer. Differences among the time series arise from: input data; quality control procedure; gridding and infilling methodology (what assumptions are made in areas of missing data); bias correction methodology; and choice of reference climatology. Anomalies are computed relative to the 1955–2002 average. Figure reproduced from Palmer et al. (2010).

The XBT-corrected OHC curves level off after 2003 (Fig. 3.9, see also Fig 3.7). Knight et al. (2009) noted a recent slowing of observed sea surface temperature rise at around the same time. However, sea level rise has continued at around 2 mm yr^{-1} since 2003 (Leuliette and Miller 2009; see also section 3h). Recent work suggests that the reduction in ocean thermal expansion over this period was partly offset by an increase in oceanic mass gain from melting terrestrial ice (Cazanave et al. 2009). Trenberth et al. (2010, see also Trenberth and Fasullo 2010) point out that melting of ice requires at least an order of magnitude less energy per unit sea level rise than ocean thermal expansion. Assuming that the top-of-atmosphere radiation balance of approximately 0.9 W m^{-2} has remained constant in recent years, an emerging issue is “where has this excess energy gone since 2003?” Deep ocean warming may account for some of the missing energy (Johnson and Doney 2006; Johnson et al. 2007; Johnson et al. 2008a). Only with a truly global ocean observing system can we close fully the global energy and sea level budgets, so we must improve our observations of the ocean below 2000 m where Argo floats currently do not reach.

The average temperature above isotherms is also immune to one known contributor to XBT bias, namely fall rate errors (e.g., Wijffels et al. 2008). By isolating the air-sea heat flux signal of ocean warming, the isotherm methodology has enabled the separate detection and attribution of volcanic and anthropogenic greenhouse gas forcings in the ocean temperature record for the first time (Palmer et al. 2009). However, due to the inherent spatial limitations, this method does not directly address the global energy budget.

The deployment of the Argo array of autonomous profiling floats over the last decade has revolutionized our ability to observe the deeper ocean (Roemmich et al. 2009). There are currently over 3000 active floats measuring temperature and salinity over the upper 2000 m every 10 days. Argo is already providing a uniformly sampled baseline for assessing past OHC changes (Lyman and Johnson 2008). A sustained Argo promises to give the detailed information on upper ocean warming that is critical to understanding the rates of global and regional climate change and for testing and improving climate models (Barnett et al. 2005). Argo data will also provide the key to initializing climate models to make better seasonal to decadal predictions in the future (Smith et al. 2007).

spheric circulation, and their changes on short- and long-term timescales have important implications for global weather and climate patterns (e.g., Emanuel 1986; Cayan 1992; Frankignoul et al. 1998).

Global estimates of daily ocean latent and sensible heat fluxes on one-degree spatial resolution are being routinely produced by the OAFlux project at Woods Hole Oceanographic Institution (Yu and Weller 2007). The computation of the OAFlux products uses the state-of-the-art bulk flux algorithm version 3.0 developed from the Coupled Ocean-Atmosphere Response Experiment (COARE) (Fairall et al. 2003), with input surface meteorological variables determined from an optimal blending of satellite retrievals (e.g., Special Sensor Microwave Imager (SSM/I), QuikSCAT, Advanced Very High Resolution Radiometer (AVHRR), and Advanced Microwave Scanning Radiometer for EOS (AMSR-E) and the surface meteorology from reanalysis/forecast models of National Centers for Environment Prediction (NCEP) and the European Center for Medium range Weather Forecasting (ECMWF).

The global latent plus sensible heat fluxes (LHF+SHF) in 2009 (Fig. 3.10a) show that, on the annual-mean basis, the largest ocean heat losses

occur over the regions that are associated with major western boundary currents (WBCs) and their extensions, such as the Kuroshio off Japan, the Gulf Stream off the United States, the Agulhas current off the African coast, the Falkland/Brazilian Current off South America, and the Eastern Australian Current. Magnitude of annual mean LHF+SHF in these regions exceeds 250 W m^{-2} , produced largely during the fall-to-winter seasons by strong winds and cold and dry air masses coming from the lands. The second largest heat loss ($\sim 180 \text{ W m}^{-2}$) is located over the broad subtropical southern Indian Ocean, where the large air-sea heat exchange is sustained primarily by the strong southeast trade winds in the monsoon months June–September. The spatial distribution of the mean global LHF+SHF field depicts a close relationship of LHF+SHF to SST and winds.

The 2009-minus-2008 difference plot of LHF+SHF (Fig. 3.10b) shows coordinated basin-scale variability with magnitude of change of the order of $\pm 50 \text{ W m}^{-2}$. One such large-scale change occurred in the tropical Pacific Ocean in association with an evolving warm phase of the ENSO phenomenon. During an El Niño, the sea surface is anomalously warm in the central and eastern equatorial basin and anomalously cool in the western basin (Fig. 3.1). The change in SST affects the near surface humidities, because saturation specific humidity goes up with temperature, and the change in sea-air humidity contrast affects latent heat flux. Hence, latent heat increased over the warm SST anomalies in the east and reduced over the cool SST anomalies in the west. The larger latent heat released from the warmer ocean surface acts to damp the positive SST anomalies, suggesting that the ocean heat flux is a key control on the persistence and amplitude of SST anomalies. Variability of ocean heat fluxes in the tropical Pacific on ENSO time scales is a dominant interannual signal (e.g., Yu and Weller 2007), and the ocean heat flux acts as a damping mechanism that regulates the growth of ENSO SST.

ENSO has far-reaching effects on global climate, and one such example is clearly demonstrated in the tropical Indian Ocean. Positive SST anomalies started to develop in the tropical Indian Ocean (IO) north of 15°S in summer 2009 after the El Niño conditions were fully established in the Pacific. The SSTs were elevated by more than 0.5°C from July to December 2009 (Fig. 3.11a). However, the basin-wide LHF *reduced* when the sea surface was warmer (Fig. 3.11b), which is in sharp contrast to the LHF increase over the warmer eastern tropical Pacific. Weaker LHF means less heat loss at the sea surface, whose effect

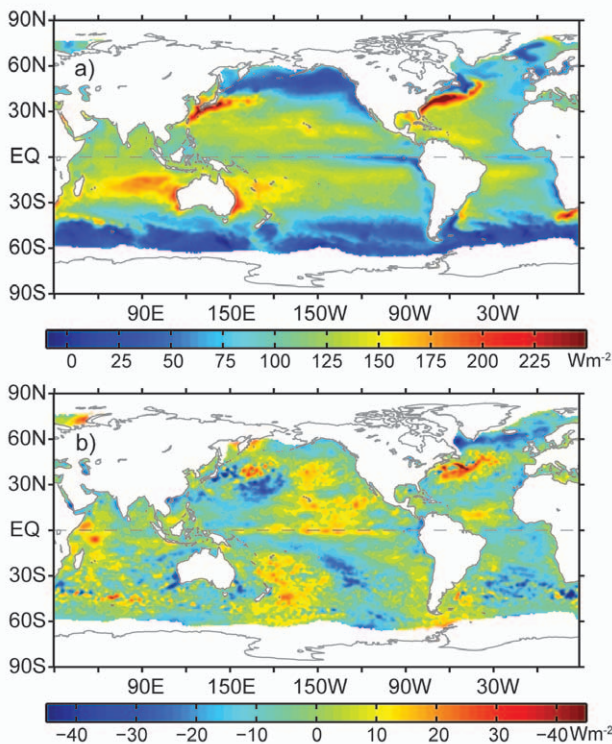


FIG. 3.10. (a) Annual mean latent plus sensible heat fluxes in 2009. The sign is defined as upward (downward) positive (negative). (b) Differences between the 2009 and 2008 annual mean latent plus sensible heat fluxes.

is to cause SST to rise if oceanic processes (e.g., mixing and advection) do not dominate. The weaker LHF was induced primarily by the weaker trade winds associated with the weakening of the Walker Circulation during El Niño, similar to the previous ENSO-induced IO warm events (Yu and Rienecker 2000). In this case, the impact of ocean heat flux was to force, not to damp, the SST anomalies.

For the Pacific Ocean, the SST 2009-minus-2008 difference map has a pattern resembling the warm phase of PDO: there is a horseshoe shaped region of negative difference anomalies surrounding a core of warmer difference anomalies to the east. The pattern suggests that the PDO phase became less negative in 2009. Indeed, the negative phase that started in September 2007 began to taper off in the first half of 2009 (<http://jisao.washington.edu/pdo/PDO.latest>) and since July 2009, the PDO index was mostly positive because of the El Niño event developing in the equatorial region during fall and winter 2009/10. The 2009-minus-2008 difference map of LHF+SHF (Fig. 3.10b) has a pattern in broad agreement with that of SST (Fig. 3.1), because the ocean heat flux responded to the SST anomalies and acted as damping to suppress the growth of SST anomalies.

Unlike the Pacific where the correlation between SST and LHF+SHF difference anomalies is *positive*, the correlation between the pair is *negative* in the Atlantic. For instance, the 2009 SSTs in the Atlantic were

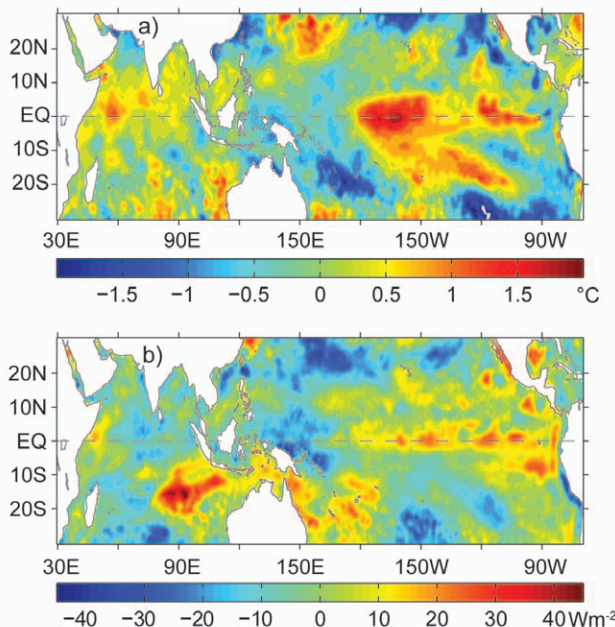


FIG. 3.11. (a) SST differences between December 2009 and July 2009 in the tropical Indo-Pacific Oceans. (b) LHF+SHF averaged over the 6 month period from July to December 2009.

predominantly cooler than the 2008 SSTs, except for the subtropical Atlantic between 15°N and 30°N and the high-northern latitudes. The surface warming in the subtropical region, together with the cooling to its north and south, was in apparent association with the NAO tripole structure. The tripole pattern is also evident in the LHF+SHF 2009–08 difference field, but positive (negative) LHF+SHF anomalies occurred mostly over cooler (warmer) sea surface. It is known that the NAO SST tripole is due primarily to the oceanic response to atmospheric forcing via the effects of the changes in LHF+SHF and surface wind induced Ekman currents (Cayan 1992; Deser and Blackmon 1993). The negative correlation between SST and LHF+SHF tripole in 2009 is consistent with the existing theory, indicating that the Atlantic basin-scale SST variability in 2009 was driven primarily by the atmospheric forcing: SST increases (decreases) as a result of reduced (enhanced) latent and sensible heat loss at the sea surface. This is seen clearly in Fig. 3.3 where a series of surface cooling episodes in the North Atlantic between 40–60°N can be well explained by the changes in the ocean heat flux.

The changing relationships between LHF+SHF and SST in the global oceans indicate that the ocean heat fluxes played a dual role in the dynamics of large-scale SST anomalies: they not only generated SST anomalies (such as in the North Atlantic and the tropical Indian Oceans) but also acted to damp SST anomalies that had already been generated (such as in the tropical and extratropical Pacific).

The long-term perspective of the change in 2009 LHF+SHF is shown in the annual mean time series averaged over the global oceans from 1958 to 2009 (Fig. 3.12). The 2009 LHF+SHF was slightly down from the 2008 mean (Peterson and Baringer 2009), continuing the downward trend that started around

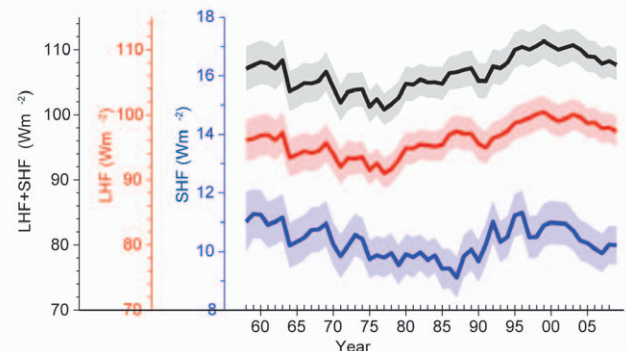


FIG. 3.12. Year-to-year variations of global averaged annual mean latent plus sensible heat flux (black curve), latent heat flux (red curve), and sensible heat flux (blue curve). The shaded areas indicate the error bars of the flux estimates at the 95% confidence level.

2000. The downward trend is driven primarily by LHF with minor positive contribution from SHF. Over the past 51 years from 1958 to 2009, the LHF+SHF time series suggests an oscillatory nature, with a low at 99 W m^{-2} in 1977 and a high at 109 W m^{-2} in 1999. The present downward trend seems to be a tendency toward reversing the upward trend that had dominated the decades of 1980s and 1990s. The accuracy of the OAFlux LHF and SHF estimates was evaluated using 105 buoys available over the global oceans (Yu et al. 2008). The averaged root-mean-square differences between OAFlux and buoy over the buoy locations are 9.6 W m^{-2} for LHF and 2.6 W m^{-2} for SHF.

e. Sea surface salinity—G. C. Johnson and J. M. Lyman

Ocean storage and transport of freshwater are intrinsic to aspects of global climate including the water cycle (e.g., Wijffels et al. 1992), El Niño (e.g., Maes et al. 2006), and anthropogenic climate change (e.g., Held and Soden 2006). Only since 2004 has the advent of the Argo array of profiling floats, that measures temperature and salinity year-round in the upper 2 km of the ice-free global ocean, nominally at 10-day intervals and $3^\circ \times 3^\circ$ spacing (Roemmich et al. 2009), allowed an annual assessment of global ocean freshwater, and its complement, salinity. Remote sensing of Sea Surface Salinity (SSS) by two satellites is anticipated in 2010 (<http://www.esa.int/esaLP/LPsmos.html>; <http://aquarius.gsfc.nasa.gov/>).

We analyze the near-global Argo data to determine an annual average SSS anomaly for 2009 relative to a climatology and to describe how annual SSS anomalies have changed in 2009 relative to 2008, as well as assessing trends in salinity since 2004 and their statistical significance. The data, downloaded from an Argo Global Data Assembly Center in January 2010, are a mix of real-time (preliminary) and delayed mode (scientific quality-controlled) data. The estimates of SSS presented could change after all the data have been subjected to careful scientific quality control.

We subject the shallowest near-surface ($< 25 \text{ m}$) salinity data flagged as good from each available Argo profile to a statistical check to discard outliers resulting in rejection of 8% of the profiles. After this check, we cast the remaining data as differences from a climatological mean surface salinity field from the 2001 World Ocean Atlas (WOA) based on historical data reported through 2001 (Boyer et al. 2002). We objectively map (Bretherton et al. 1976) the resulting anomalies for each year assuming a Gaussian

covariance function with 6° latitude and longitude decorrelation length scales and a noise-to-signal variance ratio of 2.2.

Climatological SSS patterns are correlated with surface freshwater flux: the sum of evaporation, precipitation, and river runoff (e.g., Béranger et al. 1999) where advection processes are not dominant. In each ocean basin, subtropical salinity maxima centered between roughly 20° and 25° in latitude are signatures of the predominance of evaporation over precipitation. Conversely, in most regions where climatological surface salinities are relatively fresh, such as the high latitudes and the ITCZs precipitation generally dominates over evaporation.

The 2009 SSS anomalies from WOA (Fig. 3.13a) reveal some large-scale patterns that also hold in 2004 through 2008 (Arguez 2007; Levinson and Lawrimore 2008; Peterson and Baringer 2009). The

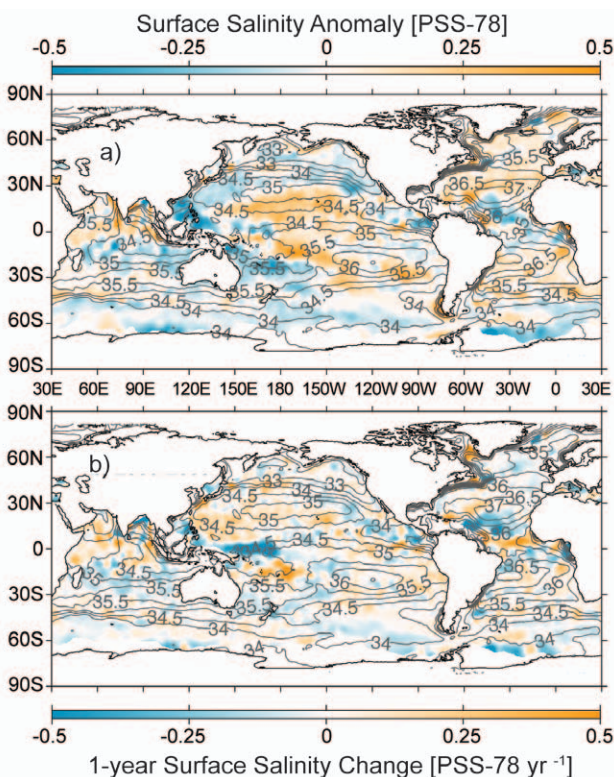


FIG. 3.13. (a) Map of the 2009 annual surface salinity anomaly estimated from Argo data [colors in PSS-78] with respect to a climatological salinity field from WOA 2001 (gray contours at 0.5 PSS-78 intervals). (b) The difference of 2009 and 2008 surface salinity maps estimated from Argo data [colors in PSS-78 yr^{-1} to allow direct comparison with (a)]. White areas are either neutral with respect to salinity anomaly or are too data-poor to map. While salinity is often reported in practical salinity units, or PSU, it is actually a dimensionless quantity reported on the 1978 Practical Salinity Scale, or PSS-78.

regions around the subtropical salinity maxima are mostly salty with respect to WOA. Most of the high-latitude climatologically fresh regions appear fresher than WOA, including most of the Antarctic Circumpolar Current near 50°S and the subpolar gyre of the North Pacific. These patterns may be consistent with an increase in the hydrological cycle (i.e., more evaporation in drier locations, and more precipitation in rainy areas), as seen in simulations of global warming. These simulations suggest this signal might be discernible over the last two decades of the twentieth century (Held and Soden 2006), consistent with the multi-year nature of these anomalies.

Nonetheless, there may be alternate explanations. It is possible that the climatology, being based on relatively sparse data distributions in many parts of the oceans, may tend to underestimate regional extrema that the well-sampled Argo array can better resolve, or that the climatology contains regional biases on seasonal or longer time-scales that are not present in the Argo data. Also, some of these patterns might be explained by interannual variability in large-scale oceanic currents or atmospheric features such as the ITCZs.

For example, in contrast to the other high-latitude areas, the subpolar North Atlantic and Nordic Seas in 2009 are anomalously salty with respect to WOA (Fig. 3.13a), as they have been since at least 2004. This salty subpolar anomaly is inconsistent with a simple increase in the strength of the hydrological cycle. However, the pattern appears mostly due to northward spread of saltier subtropical waters from the south into the northeastern North Atlantic since the mid-1990s (Holliday et al. 2008; Hakkinen and Rhines 2009). This trend towards increasing salinity in the region may have halted or even reversed recently, since salinities in the area freshened slightly from 2008 to 2009 (Fig. 3.13b) and show no large-scale significant trend since 2004 (Fig. 3.14).

Salinity in the tropics exhibits strong interannual variability owing to influences of phenomena such as the ENSO cycle (e.g., Ando and McPhaden 1997). For instance, the western equatorial Pacific fresh pool spread eastward from 2008 to 2009 (Fig. 3.13b), with the freshening in this region at least partly owing to anomalous eastward currents along the equator (Fig. 3.15) in the presence of the mean zonal salinity gradient there. In contrast, the Atlantic ITCZ became saltier. In addition, the strong fresh anomaly found south of India in the tropics in 2006 (Arguez 2007) has steadily weakened over the past few years (Levinson and Lawrimore 2008; Peterson and Baringer 2009)

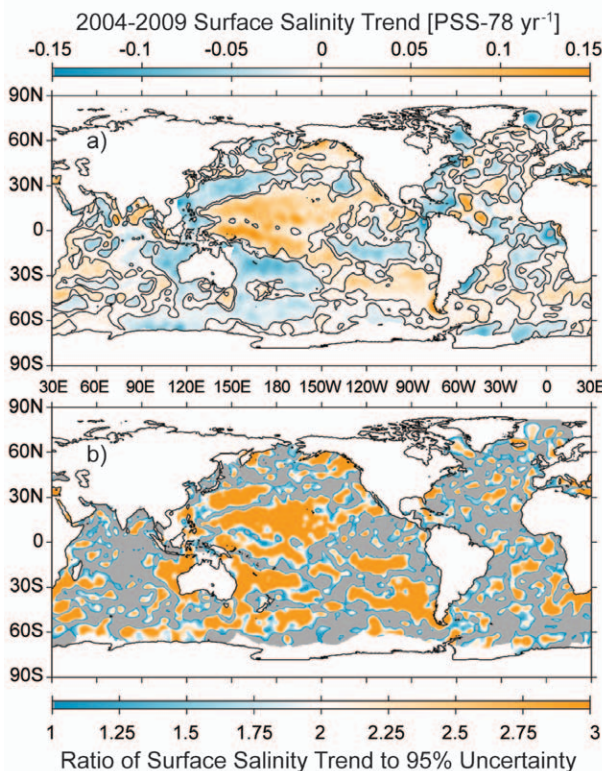


FIG. 3.14. (a) Map of local linear trends estimated from annual surface salinity anomalies for the years 2004–09 estimated from Argo data (colors in PSS-78 yr^{-1}). (b) The ratio of these trends to estimates of the 95% confidence interval, with grey regions showing areas without statistically significant trends and colors from blue to orange indicating increasing statistical significance of the trends.

and is now absent in 2009. Tropical salinity changes from 2008 to 2009 (Fig. 3.13b) show some visual similarities with changes in latent and short wave heat fluxes between the years (Fig. 3.10b), as might be expected given the relation of these parameters to evaporation.

We estimate linear trends from 2004–09 (Fig. 3.14a), since Argo coverage became near global in 2004, and the ratio of these trends to their 95% significance (Fig. 3.14b). The most striking trend patterns are in the Pacific. Saltier surface values in the western and central tropical Pacific extend into the eastern Pacific subtropics in both hemispheres. A strong freshening also occurs in the western subtropics of each hemisphere in the Pacific and the far western tropical Pacific, extending into the Indian Ocean northwest of Australia. The other large-scale patterns include freshening in the tropical Southeast Pacific and along the equatorial Atlantic.

f. Surface currents—R. Lumpkin, G. Goni, and K. Dohan

Near-surface currents are measured in situ by drogued satellite-tracked drifting buoys and by current meters on moored Autonomous Temperature Line Acquisition System (ATLAS) buoys.¹ During 2009, the drifter array ranged in size from a minimum of 778 drogued buoys to a maximum of 1149, with a median size of 937 drogued buoys (undrogued drifters continue to measure SST, but are subject to significant wind slippage; Niiler et al. 1987). The moored array included 38 buoys with current meters, all between 12°S and 21°N. These tropical moorings compose the Tropical Atmosphere Ocean (TAO; Pacific), Pilot Research Moored Array in the Tropical Atlantic (PIRATA; Atlantic) and Research Moored Array for African–Asian–Australian Monsoon Analysis and Prediction (RAMA; Indian) arrays.

Satellite-based estimates of ocean currents are produced using several methodologies, including the OSCAR (Ocean Surface Current Analyses–Real time) project, which uses satellite altimetry, winds, SST, and the Rio05 mean dynamic topography from the AVISO Ssalto/Duacs multimission altimeter gridded product (Rio and Hernandez 2004) to create one-degree resolution surface current maps averaged over the 0–30 m layer of the ocean (Bonjean and Lagerloef 2002). Anomalies are calculated with respect to the time period 1992–2007.

1) PACIFIC OCEAN

In the equatorial Pacific, the year began with a tapering off of the westward surface current anomalies at the end of 2008 (Fig. 3.15), bringing currents back to their climatological January values, although SST anomalies remained cold until April (Fig. 4.1). By February, eastward surface current anomalies were present on the equator from 160°E to 100°W. This El Niño pattern developed and intensified through May. In June–August, this pattern weakened in the central part of the basin, and near-climatological currents (or even westerly anomalies) were seen from the dateline to 120°E. The El Niño eastward anomalies began

¹ Drifter data is distributed by NOAA/AOML at <http://www.aoml.noaa.gov/phod/dac/gdp.html>. Moored data is distributed by NOAA/PMEL at <http://www.pmel.noaa.gov/tao>. OSCAR gridded currents are available at <http://www.oscar.noaa.gov/> and <http://podaac.jpl.nasa.gov/>. AVISO gridded altimetry is produced by SSALTO/DUACS and distributed with support from CNES, at <http://www.aviso.oceanobs.com/>. Analyses of altimetry-derived surface currents are available at <http://www.aoml.noaa.gov/phod/altimetry/cvar>.

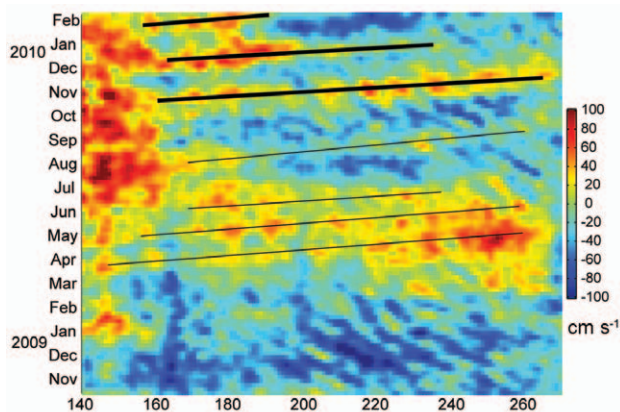


FIG. 3.15. Time-longitude plot of anomalous zonal equatorial currents (cm s^{-1}) from OSCAR. Black lines indicate eastward anomalies associated with propagating Kelvin waves.

redeveloping in August, in the form of eastward propagating Kelvin wave pulses that are concurrent with westerly wind anomalies (Fig. 3.15). Two major wave trains were generated at the start of October and December, resulting in strong eastward anomalies west of 140°E in October. In November through December, eastward anomalies dominated the entire equatorial band of the Pacific Ocean (Fig. 3.16).

Surface current anomalies in the equatorial Pacific typically lead SST anomalies by several months, with a magnitude that scales with the SST anomaly magnitude. Recovery to normal current conditions is also typically seen before SST returns to normal. Thus, current anomalies in this region are a valuable predictor of the evolution of SST anomalies and their related climate impacts. This leading nature can be

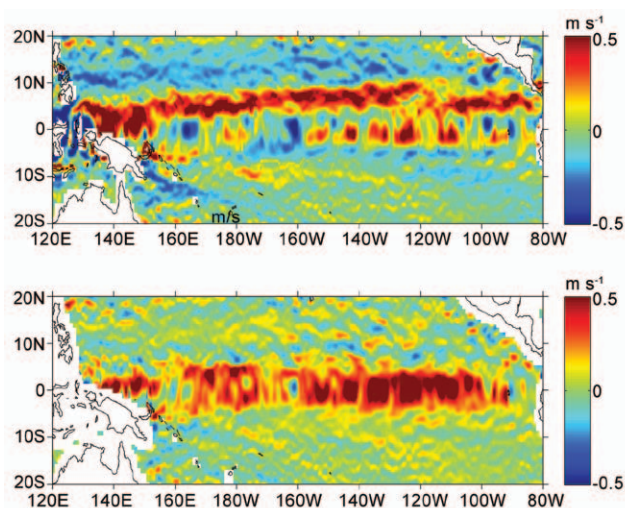


FIG 3.16. November 2009 zonal currents (top) and zonal current anomalies (bottom) in m s^{-1} , from OSCAR. Eastward anomalies exceeding 50 cm s^{-1} dominated most of the equatorial Pacific.

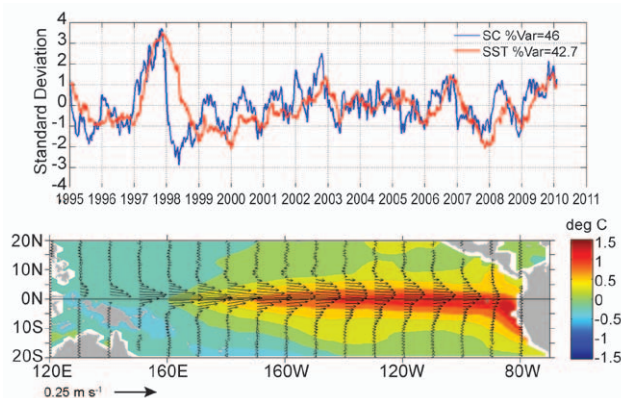


FIG 3.17. Principal empirical orthogonal functions (EOF) of surface current (SC) and of SST anomaly variations in the Tropical Pacific. (top) Amplitude time series of the EOFs normalized by their respective standard deviations. (bottom) Spatial structures of the EOFs.

seen clearly in the first principal EOF of surface current anomaly and separately of SST anomaly in the tropical Pacific basin (Fig. 3.17). By the end of 2009, the values of the normalized surface current and SST EOFs were reaching values approaching those of the 2002 El Niño, the strongest El Niño since the massive 1997–98 event.

The year ended with another strong wave pulse at the beginning of January 2010, together with a southward shift in westerly wind anomalies (Fig. 4.4), often associated with the onset of the termination of El Niño conditions (Lagerloef et al. 2003).

2) INDIAN OCEAN

The Agulhas Current in the southwestern Indian Ocean is the major western boundary current linking the Indian and South Atlantic basins. Its transport can be estimated on a monthly basis using a combination of altimetry and hydrographic climatology (see <http://www.aoml.noaa.gov/phod/altimetry/cvar/index.php>). In 2009, the baroclinic transport of the Agulhas decreased from a maximum seen in 2007, to $\sim 48 \text{ Sv}^2$, a value similar to those of the 1993–2000 period (Fig. 3.18, top). The generation of Agulhas rings, which carry Indian Ocean water into the Atlantic, decreased from the peak seen during 2007/08 (Fig. 3.18, bottom) to the more typical long-term average of $\sim 5 \text{ rings yr}^{-1}$.

3) ATLANTIC OCEAN

In the tropical Atlantic, 2009, surface currents were close to climatology except during boreal spring.

Eastward anomalies of up to 50 cm s^{-1} occurred along the equatorial Atlantic in April through May, in response to weaker than normal Trade Winds that were also associated with anomalously cold SSTs in the northeastern Tropical Atlantic. This eastward anomaly pattern was disrupted in June–July, when westward anomalies developed east of 20°W in the Guinea Current region. By July, these currents had returned to normal climatological values.

Against the east coast of South America, the southward-flowing warm, salty Brazil Current meets the northward flowing cold, fresh Malvinas Current to create the Confluence Front.

Over the last 15 years, the location of this front has shifted to the south at a mean speed of nearly 1° latitude per decade (Goni et al. 2010, manuscript submitted to *Deep-Sea Res.*; Lumpkin and Garzoli 2010, manuscript submitted to *J. Geophys. Res.*). However, most of this shift occurred in the early part of the altimeter-derived time series; while it exhibits strong intraseasonal to seasonal fluctuations (Goni and Wainer 2001), its annual-averaged position has not changed significantly since 1998, and in 2009 it fluctuated between 37° and 39°S .

g. The meridional overturning circulation—M. O. Baringer, T. O. Kanzow, C. S. Meinen, S. A. Cunningham, D. Rayner, W. E. Johns, H. L. Bryden, J. J.-M. Hirschi, L. M. Beal, and J. Marotzke

The meridional redistribution of mass and heat associated with the large-scale vertical circulation within the oceans is typically called the meridional overturning circulation (MOC). The most common definition of the strength of the MOC at any particular latitude is the maximum of the vertically integrated basinwide stream function, which changes as a function of latitude and time and is influenced by many physical systems embedded within it. There are several available estimates of the steady-state global mass, fresh water, and heat transport based on the best available hydrographic data (Talley 2008; Lumpkin and Speer 2007; Ganachaud and Wunsch 2003), as well as a few local estimates of the MOC from one-time full water column hydrographic sections and western boundary arrays (e.g., McDonagh et al. 2008; Kanzow et al. 2008); however, true time-series observations of basinwide MOC transports are logistically very challenging to collect.

Substantial progress has been made on developing a coordinated observing system to measure the MOC through the international conference called OceanObs09 held September, 2009. The conference resulted in numerous community white papers and

² Sv is a Sverdrup or $10^6 \text{ m}^3 \text{ s}^{-1}$, a unit commonly used for ocean volume transports.

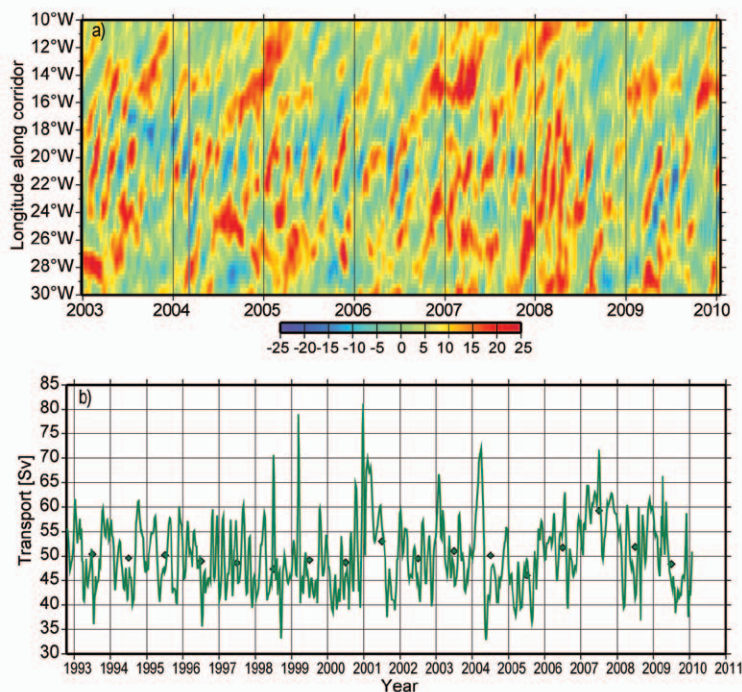


FIG. 3.18. (a) Time–longitude plot of sea height anomaly (SHA) in cm along the corridor of Agulhas ring propagation into the Atlantic Ocean, showing the presence of rings as high SHA (red colors). (b) monthly transport of the Agulhas Current (solid line) and annual averages (dots).

conference summary papers aimed at synthesizing recommendations for a sustained observing system including measurements of the MOC (e.g., Cunningham et al. 2010; Rintoul et al. 2010). Presently, quantifying changes in the complex, global MOC are being inferred only from observations of one component of the MOC (e.g., a specific current or ocean layer; e.g., Kanzow et al. 2008), at discrete locations (e.g., at 26.5°N in the Atlantic; Cunningham et al. 2007; Kanzow et al. 2007; Johns et al. 2008), or from indirect measurements such as air-sea fluxes thought to force the MOC (e.g., Marsh 2000; Speer 1997), or indirect measurements thought to be influenced by changes of the MOC, such as deep property fields like temperature or salinity (e.g., Johnson et al. 2008b). A prototype for the recommended observing system has been in place since April 2004, spanning the subtropical gyre in the North Atlantic near 26.5°N, hence this note concentrates on those observations. The system is composed of UK-NERC RAPID MOC moorings, US-NSF Meridional Overturning Circulation Heat-Transport Array (MOCHA), and the US-NOAA Western Boundary Time Series program (see Kanzow et al. 2007; Kanzow et al. 2008; Cunningham et al. 2007).

The most up-to-date estimates of the MOC from the 26.5°N array include data from April 2004 to April 2008³ (Cunningham et al. 2007; Kanzow et al. 2010, manuscript submitted to *J. Climate*). Over this time period the MOC has averaged 18.7 Sv with a high of 32.1 Sv, a low of 3.2 Sv, and a standard deviation of 4.8 Sv (using the twice daily values filtered with a 10-day cutoff as described in Cunningham et al. 2007). The data suggest no significant trend in the strength of the MOC. After four years of data, a seasonal signal is beginning to emerge (Fig. 3.19) with a low MOC in April and a high MOC in October and peak to trough range of about 7 Sv. The MOC can be divided into three components: the northward western boundary Florida Current, the wind-driven Ekman transport, and the southward “interior” transport (upper ocean geostrophic flow between the Bahamas and Africa). The seasonal cycle of the MOC appears to be largely attributable to seasonal variability in the interior rather than Ekman or Florida Current fluctuations (Kanzow et al. 2010, manuscript submitted to *J. Climate*). Of note is that all the MOC transport values estimated from five repeated CTD sections by Bryden et al. (2005) can be found within the seasonal range of the MOC time series (values ranged from 22.9 Sv in 2004 to 14.8 Sv in 1957). These results do not disprove the presence of a long-term trend in the strength of the MOC (e.g., as suggested by Bryden et al. 2005; Wunsch and Heimbach 2006), but they do suggest that a careful error analysis must be performed that includes the impact of the underlying higher-frequency variability of the MOC on trend estimates (e.g., Baehr et al. 2008; Baehr et al. 2007; Brennan et al. 2008). Other related studies of the MOC trend are, so far, contradictory with some reporting a decrease in the MOC or components of the MOC (e.g., Wunsch and Heimbach 2006; Longworth et al. 2010, unpublished manuscript) while others suggest no change or even an increase (e.g., Köhl and Stammer 2008; Zhang 2008; Olsen et al. 2008; Lumpkin et al. 2008; Schott et al. 2009). Clearly, while disagreement remains over the details of findings from any particular observing systems (e.g., Kanzow et al. 2009), agreement exists

³ Observations of the strength of the MOC from the 26.5° mooring array are available only with a time delay as the moorings are recovered over 12 to 18 month intervals.

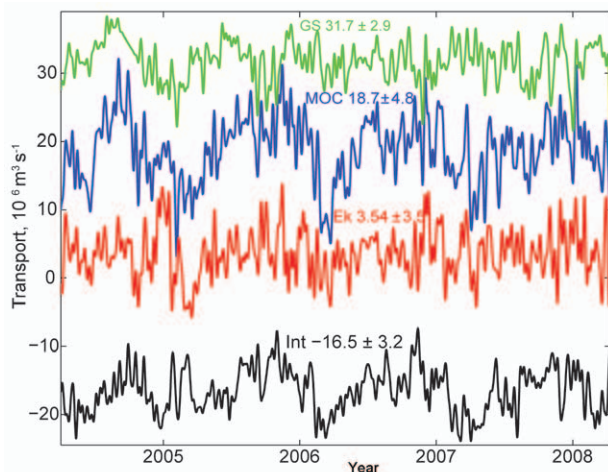


FIG. 3.19. Daily estimates of the strength of the meridional overturning circulation (MOC; blue line) and its components, the Florida Current (GS: green), wind-driven Ekman transport (Ek: red) and the geostrophic interior (Int: black), as measured by the United Kingdom's National Environmental Research Council (NERC) Rapid Climate Change Program, the National Science Foundation's Meridional Overturning and Heat transport Array, and the long-term NOAA funded Western Boundary Time Series Program. The interior volume transport estimate (accurate to 1 Sv, Cunningham et al. 2007) is based on the upper-ocean transport from April 2004 to April 2008 (see also Kanzow et al. 2009), with a 10 day low-pass filter applied to the daily transport values.

that longer time series at multiple locations, particularly of the deep transport components, is needed (e.g., Wunsch 2008).

One of the main components of the MOC estimate near 26.5°N is the Florida Current transport, the longest transport time series of an ocean circulation feature directly linked to the MOC. Near this latitude in the Atlantic the bulk of the warm upper limb of the Atlantic MOC is thought to be carried in the Florida Current through the Straits of Florida and the majority of the cold lower limb is believed to be carried to the south in the Deep Western Boundary Current (DWBC) just east of the Bahamas (e.g., Baringer and Larsen 2001; Meinen et al. 2010). Since 1982, variations in an important contributor to the upper limb of the Atlantic MOC have been monitored by measuring the Florida Current transport using a submarine cable across the Straits of Florida in combination with regular hydrographic sections. In 2009 the median transport through the Florida Straits was $31.3 \pm 1.2 \text{ Sv}^4$, slightly lower than the $31.7 \pm 2.2 \text{ Sv}$ median transport in 2008, but well within the middle range

of mean annual values (32.2 Sv median transport of the Florida Straits from 1982 to 2008 with 50% of the annual means within $\pm 2.2 \text{ Sv}$). There were, however, several unusual high-frequency events during the year (Fig. 3.20): anomalously low-transport (outside of two standard deviations of the daily averaged values) events during 20–22 May, 18–27 June, 14–15 November, and 21–22 December, with values as low as about 23 Sv and an unusually high transport 11–12 July, with values as high as about 38 Sv. Due to the fact that these events were relatively short-lived, it is likely they are local responses to atmospheric forcing and coastally trapped wave processes and are not particularly indicative of a climatically-important shift (e.g., Mooers et al. 2005). However, these transient fluctuations can have important environmental consequences. In the summer of 2009, the east coast of the United States experienced a high sea level event that was unusual due to its unexpected timing, large geographic scope, and coastal flooding that was not associated with any storms (Sweet et al. 2009). Sweet et al. (2009) showed that this anomalous event was related to the anomalously low Florida Current transport: a reduced Florida Current transport corresponds to a lower sea surface height gradient across the front and hence higher sea level onshore. Changes in Florida Current transport and the associated MOC have been similarly shown to affect sea level along the east coast of the United States through other studies such as Bingham and Hughes (2009) and Yin et al. (2009).

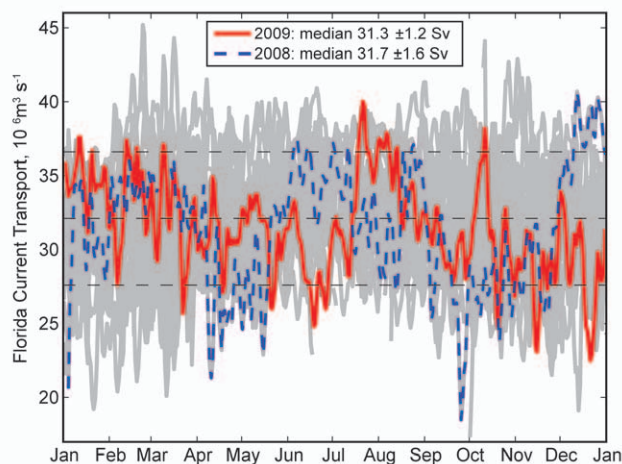


FIG. 3.20. Daily estimates of the transport of the Florida Current during 2009 (red solid line) compared to 2008 (dashed blue line). The daily values of the Florida Current transport for other years since 1982 are shown in light grey. The median transport in 2009 decreased slightly relative to 2008, and is slightly below the long-term median for the Florida Current (32.2 Sv).

⁴ Standard error of the mean represents 95% confidence limits.

Trends in the MOC can also be determined through proxies of the MOC strength, such as paleo observations (e.g., Carlson et al. 2008), tracers (e.g., LeBel et al. 2008), and water mass characteristics (e.g., Kouketsu et al. 2009; Lohmann et al. 2008; Hawkins and Sutton 2007). For example during the past year, temperature and salinity observations in the Labrador Sea showed an abrupt return of deep convection between 2007 and 2008 (Våge et al. 2009). Yashayaev and Loder (2009) showed that the enhanced deep convection in the Labrador Sea in the winter of 2008 was the deepest since 1994 and included the largest heat loss from the ocean to the atmosphere since the mid-1990s, exceeding the long-term mean by 50%. Such anomalous local events may be a precursor to changes in the MOC strength (e.g., Lohmann et al. 2009; Bellucci et al. 2008). Large-scale changes in temperature and salinity can also provide an indication of circulation changes; for example, Kouketsu et al. (2009) and Johnson et al. (2008a) showed that deep water temperature changes are consistent with a slowing of the deep circulation.

h. Sea level variations—M. Merrifield, S. Gill, E. Leuliette, L. Miller, G. Mitchum, S. Nerem, and P. Woodworth

The dominant changes in sea level during 2009 were associated with a moderate El Niño event that peaked at the end of the year. We first describe quarterly sea level anomalies, which illustrate the sea level signature of the El Niño event, followed by the 2009 annual mean relative to a long-term mean and to the 2008 mean, which we treat as the present sea level tendency. We conclude with an update on global sea level rise and a brief description of daily sea level extremes observed at coastal and island tide gauges in 2009.

The La Niña event that developed in 2007 and persisted through 2008 was still evident during January–February–March 2009 (JFM 09) with high/low sea surface height (SSH) anomalies in the western/eastern tropical Pacific (Fig. 3.21). Positive anomalies extended throughout the Indonesian Archipelago into the tropical Indian Ocean and southward along the west coast of Australia. The La Niña weakened noticeably along the western equatorial Pacific during April–May–June 2009 (AMJ

09) with the excitation of a downwelling Kelvin wave that created positive SSH anomalies in the central and eastern equatorial Pacific. The size of the positive SSH anomalies in the western Pacific warm pool region also began to diminish during AMJ 09 presumably due to weakening trade winds to the east. The high SSH anomalies in the eastern tropical Pacific increased in amplitude during July–August–September 2009 and peaked in October–November–December 2009 (OND 09). By OND 09 the high water levels in the western equatorial Pacific had largely subsided to background levels with the exception of a branch of high water level near the South Pacific Convergence Zone. Most of these changes in equatorial sea level are associated with changes in regional ocean heat content (see section 3c.).

Averaged over the entire year, the SSH anomaly includes contributions from the weakening La Niña state and the strengthening El Niño with high water levels across the equatorial Pacific (Fig. 3.22, top panel). The low levels along the Pacific coast of North America with high levels in the central North Pacific suggest the dominance of the negative phase of the PDO. High anomalies occur along the paths of the Gulf Stream and Kuroshio extensions, suggesting either a strengthening or meridional shift of those currents. In general, sea level appears to be unusually high in the Indian Ocean relative to the 1993–2002 baseline with the exception of the mid- to high-latitude North Pacific and North Atlantic and in the

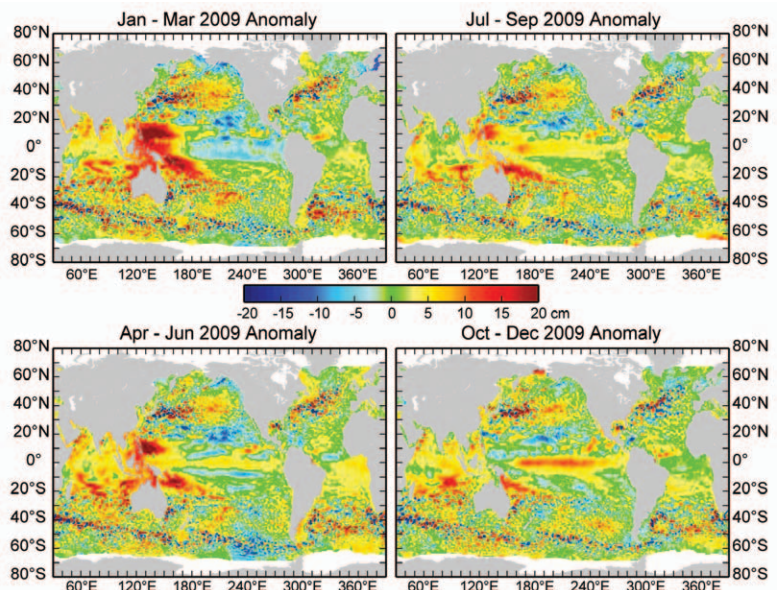


FIG. 3.21. Seasonal SSH anomalies for 2009 relative to the 1993–2007 baseline average are obtained using the multimission gridded sea surface height altimeter product produced by Ssalto/Duacs and distributed by Aviso, with support from CNES (www.aviso.oceanobs.com).

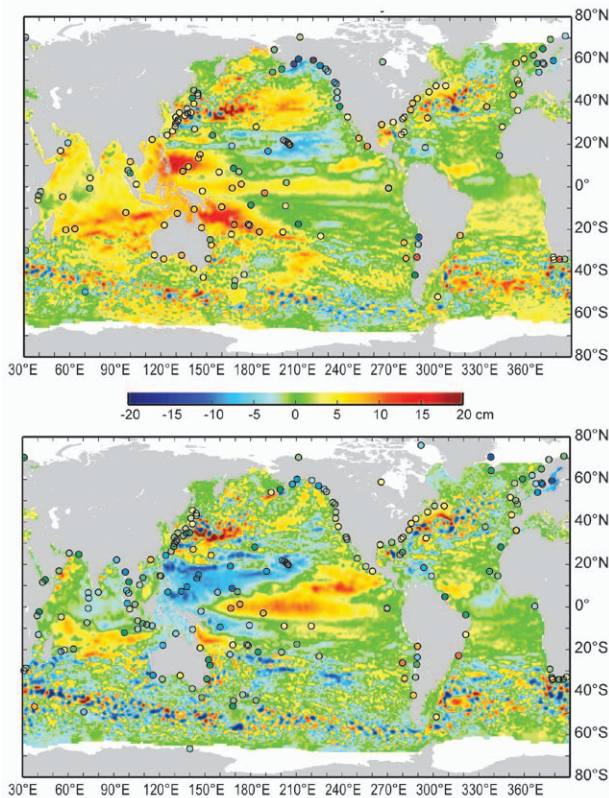


FIG. 3.22. (top) The 2009 SSH anomaly (Ssalto/Duacs product) from the 1993-2007 baseline is compared to the 2009 anomaly computed for tide gauge data (dots) obtained from the University of Hawaii Sea Level Center (<http://uhslc.soest.hawaii.edu/>). (bottom) The difference between 2009 and 2008 annual means.

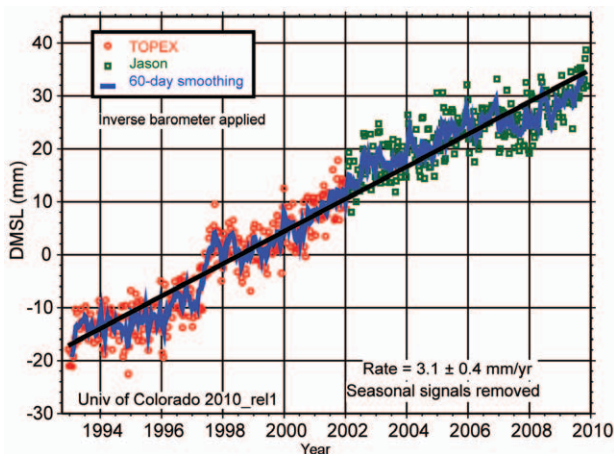


FIG. 3.23. Global mean sea level time series provided by S. Nerem, University of Colorado at Boulder. The rate does not include the global isostatic adjustment correction, which nominally adds 0.3 mm yr^{-1} to the rate. Information on how the time series was constructed is available at <http://sealevel.colorado.edu/documents.php>.

southern tropical Atlantic. The coastal tide gauge and SSH levels are similar at most stations.

The SSH tendency (Fig. 3.22, bottom panel) shows the seesaw shift in water levels in the tropical Pacific caused by the El Niño event. SSH tended to drop in the Indian Ocean, except for a band south of the equator extending from Australia to Madagascar. Levels along the coast of Australia decreased from 2008 to 2009 due to the propagation of upwelling variable Kelvin waves along the coast during the El Niño event.

The rate of global mean sea level (GMSL) rise is estimated currently to be $3.1 \pm 0.4 \text{ mm yr}^{-1}$ (3.4 mm yr^{-1} with correction for global isostatic adjustment) (Fig. 3.23). Nerem et al. (2010, manuscript submitted to *Marine Geodesy*) and Leuliette and Scharroo (2010, manuscript submitted to *Marine Geodesy*) provide recent updates of the GMSL trend calculation. Variations in GMSL about the long-term trend tend to correlate with ENSO. This is evident as GMSL dips below the long-term trend during the 2007–08 La Niña event and returns to the long-term trend with perhaps slightly higher values during the latter part of 2009 and the current El Niño event. Because of the combination of the trend and the El Niño, GMSL levels at the end of 2009 were generally the highest over the length of the altimeter record.

Variations in GMSL due to changes in ocean density (steric sea level) and ocean mass are currently under investigation using satellite altimeters, the Argo array (measuring ocean temperature and salinity), and the Gravity Recovery and Climate Experiment (GRACE) time series (measuring ice melt and other hydrological variations). An update to the analysis of Leuliette and Miller (2009) using an additional year of steric observations from Argo profiles and ocean mass variations from the GRACE gravity mission of sea level continues to show that the sea level rise budget can be closed within the range of uncertainties (Fig. 3.24). For the period January 2004 to March 2009, total sea level rise measured by the Jason-1 and Jason-2 altimeters is 2.7 mm yr^{-1} . In areas more than 200 km from the nearest coast, the altimeter rate is $1.8 \pm 1.1 \text{ mm yr}^{-1}$, while the combination of the steric and ocean mass components is $1.4 \pm 0.6 \text{ mm yr}^{-1}$ or $2.3 \pm 0.6 \text{ mm yr}^{-1}$, depending on the choice of a glacial isostatic adjustment correction.

Extreme water levels during 2009 are examined using daily averages obtained from a global set of tide gauges (Fig. 3.25). Extreme levels, taken as the average of the 2% highest daily values relative to the annual mean level (top panel), were high along the coasts of North America, Europe, South Australia, and in the

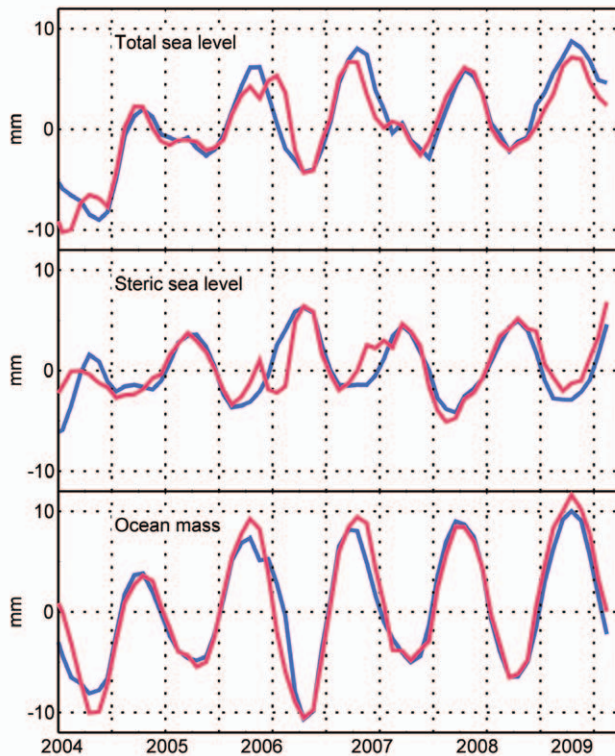


FIG. 3.24. Time series of GMSL, or total sea level, is compared with the two principal components of sea level change, upper-ocean steric change from Argo measurements, and mass change from GRACE measurements (update of Leuliette and Miller 2009). In this figure, blue lines show the observed values and red lines show the inferred values from the complementary observations (e.g., the inferred steric sea level is obtained from observed total sea level minus observed ocean mass).

eastern Bay of Bengal. For time series with at least 15 years of record length, we normalize the levels by removing the mean and dividing by the standard deviation of extreme sea levels for all available years (Fig. 3.25, bottom panel). By this measure, extremes along the east coast of the United States (see Sweet et al. 2009 for a description of the summer 2009 sea level anomalies in this region), the south coast of Alaska, and at South Africa were notably higher than normal. Other areas of unusually high values include eastern and southern Australia and isolated stations in Hawaii and the South Pacific. Extremes were generally below normal along the west coast of Canada, at Chile, Scandinavia, Thailand, and at island stations in the western equatorial Pacific.

i. The global ocean carbon cycle—C. L. Sabine, R. A. Feely, R. Wanninkhof, T. Takahashi, S. Khatiwala, and G.-H. Park

1) CARBON DIOXIDE FLUXES

Global ocean surface ocean CO₂ levels are extremely variable in space and time, especially on seasonal time scales. To document the changing patterns of air-sea CO₂ exchange requires an extensive observational program. The latest global flux map, based on a compilation of approximately three million measurements collected between 1970 and 2007, provides information on the monthly patterns of air-sea fluxes during a “normal” non-El Niño year taken to be 2000 (Takahashi et al. 2009a). The number of annual surface CO₂ observations has been growing exponentially since the 1960s such that today well over one million observations are reported to data centers each year. This tremendous increase in the number of annual observations provides exciting opportunities to look at the patterns of air-sea CO₂ fluxes in greater detail to understand the seasonal to interannual variations and the mechanisms controlling them. As a compliment to Takahashi’s work

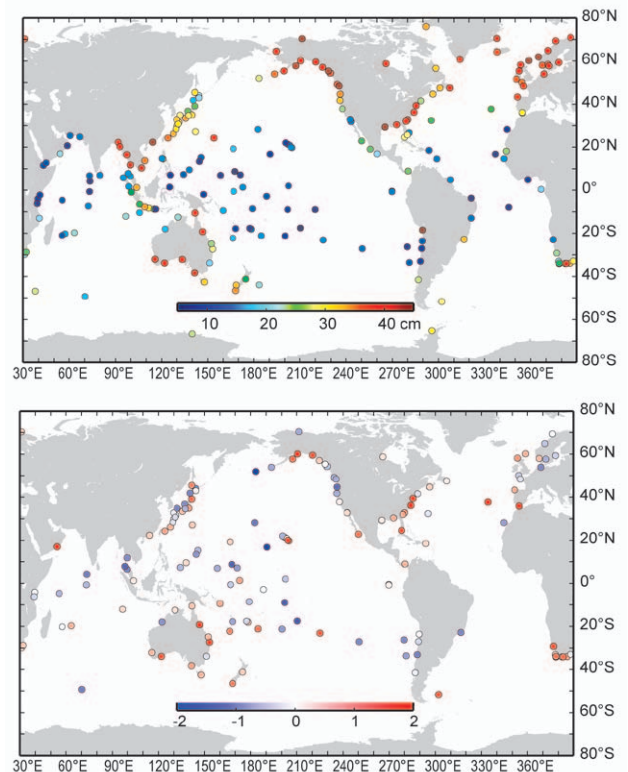


FIG. 3.25. (top) Extreme sea level variability is characterized using the average of the top 2% mean daily sea levels during 2009 relative to the annual mean at each station. (bottom) The extreme values are normalized by subtracting the mean and dividing by the standard deviation of past year extreme values for stations with at least 15-year record lengths.

to update the CO₂ climatology, there is an ongoing international effort to synthesize all the available surface CO₂ data into a quality controlled database that can be used to examine surface CO₂ variability over a range of time and space scales (SOCAT; <http://www.socat.info/>).

Over the last few years, we have presented annual global air-sea CO₂ flux estimates based on empirical approaches relating in situ measurements with satellite observations of wind and sea surface temperature (Sabine et al. 2008, 2009). The latest empirical approach for quantifying the air-sea CO₂ exchange utilizing in situ, climatological, and satellite data is described in Park et al. (2010, manuscript submitted to *Tellus B*). Lags in availability of quality controlled data streams including atmospheric CO₂, satellite and assimilation products preclude real-time analysis such that consistent, climate quality seasonal air-sea CO₂ flux maps are only available through 2008. The global mean air-sea CO₂ flux for the period from 1982 to 2008 gives an average contemporary net uptake of 1.48 Pg (10¹⁵ g) C yr⁻¹. Following the Gruber et al. (2009) assumption that the preindustrial steady state ocean was a source of 0.45 Pg C yr⁻¹, the estimated average flux equates to a net ocean anthropogenic CO₂ uptake of 1.93 Pg C yr⁻¹, consistent with the range of estimates (1.8–2.4 Pg-C yr⁻¹) recently summarized by Gruber et al. (2009).

Using the Park et al. (2010, manuscript submitted to *Tellus B*) approach the global net uptake flux for 2008 is estimated to be 1.23 Pg C yr⁻¹, 0.25 Pg C yr⁻¹ smaller than the 27-year long-term average (Fig. 3.26). The uncertainty of the empirical flux estimates is difficult to evaluate as discussed in detail in Park et

al. (2006), but the 2008 uptake is significantly lower than the 1 σ interannual variability estimate of ± 0.14 Pg C yr⁻¹ for the whole record. Compared to long-term average fluxes, 2008 generally showed less CO₂ uptake and more CO₂ release with a few notable exceptions including the high-latitude North Atlantic, the eastern subtropical North Pacific, and portions of the Southern Ocean. Greater CO₂ efflux was found in the Equatorial Pacific due to the strengthened upwelling of deep water rich in CO₂. As noted by Takahashi et al. (2009a) the 2008 flux estimates also show areas near 60°S located along the edge of the seasonal sea-ice field had less uptake of CO₂ in summer time and more release of CO₂ in winter time. Despite a band of increased CO₂ uptake in the eastern North Pacific, overall the North Pacific uptake was lower in 2008 relative to the long-term average.

Several recent publications have described regional variations in CO₂ uptake patterns, particularly in the North Atlantic and Southern Ocean, as the ocean carbon community works to distinguish secular trends from natural interannual variations (e.g., LeQuere et al. 2009; Watson et al. 2009; Metzl 2009; Lenton et al. 2009). For example, recent observations suggest a rapid decrease in the CO₂ uptake in the temperate North Atlantic. However, Thomas et al. (2008) used a general circulation model study to infer that the North Atlantic CO₂ uptake may increase again when the NAO returns to a positive state, similar to the early 1990s.

The empirical approach for evaluating the annual CO₂ flux gives an estimated interannual variability of ± 0.14 Pg C yr⁻¹ over the last three decades. While variability in the North Atlantic and Southern Ocean are observed in our analyses, the largest interannual variations are associated with ENSO changes. A negative correlation ($R^2 \sim 0.68$) is observed in a plot of the yearly Multivariate ENSO Index (MEI) values versus the annual global air-sea CO₂ uptake estimates for the period from 1982 to 2008 (Fig. 3.27). A negative MEI value indicates La Niña conditions and thus enhanced CO₂ outgassing in the Equatorial Pacific. In last year's report we described the CO₂ flux patterns associated with the moderate 2007 La Niña (Sabine et al. 2009). The conditions described here for 2008 reflect the second strongest La Niña conditions in the 27-year record and show an overall global ocean flux response of increased outgassing that was consistent with these conditions (Fig. 3.27).

In 2009, the ENSO switched from La Niña to El Niño conditions (chapter 4b). Interestingly, both ship-board measurements and moored CO₂ observations

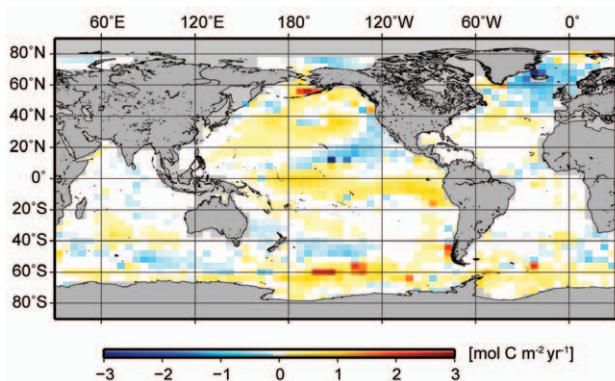


FIG. 3.26. Global distribution of air-sea CO₂ flux anomalies in 2008 compared to 27-year mean values as calculated using the Park et al. (2010, manuscript submitted to *Tellus B*) approach. Positive values indicate less uptake or more release of CO₂ by the ocean. Fluxes are not determined for the gray regions.

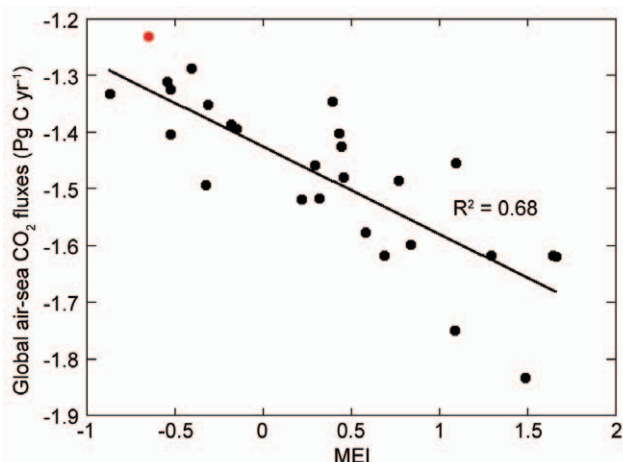


FIG. 3.27. Correlation between global air-sea CO₂ fluxes and the Multivariate ENSO Index (MEI). The red dot indicates 2008 value.

along the equator are showing a pattern of sustained CO₂ outgassing even in the presence of significant positive temperature anomalies. This switch to El Niño conditions was too recent to evaluate with the climate quality seasonal CO₂ flux maps, but preliminary estimates based on lower quality remotely sensed data are available to within three months of present (see <http://cwcgom.aoml.noaa.gov/erddap/griddap/aomlcarbonfluxes.graph>). These preliminary results also suggest that large-scale equatorial fluxes are not following the historical El Niño patterns.

The empirical CO₂ flux model generally agrees well with GCM models in both the timing and magnitude of the Equatorial Pacific flux anomalies associated with ENSO (Fig. 3.28). However, the correlation did not hold with the latest El Niño in 2002. The GCM model suggested a significant decrease in outgassing from the Equatorial Pacific which would be expected from the El Niño conditions, but did not seem to be reflected in the in situ observations or the empirical model (Fig. 3.28). The mechanisms responsible for the break down in correlation between the El Niño and the CO₂ during this last El Niño event are being investigated, but the pattern seems to be repeating with this current 2009/10 El Niño. It could be related to the relative roles of horizontal advection versus vertical advection when the warming is focused on the Central Pacific compared to the Eastern Pacific but the data collected during the 2009/10 event will help us to better understand these mechanisms.

2) SUBSURFACE CARBON INVENTORY

In the 1990s carbon samples were collected and analyzed from approximately 95 research cruises run as part of the international World Ocean Circulation

Experiment (WOCE) and the Joint Global Ocean Flux Study (JGOFS). Based on these data, Sabine et al. (2004) estimated that the total inventory of anthropogenic CO₂ in the ocean (C_{ant}) in the year 1994 was 118±19 Pg C, accounting for 48% of the CO₂ released from fossil fuel burning between 1800 and 1994. This one-time global survey, however, could not provide information on how ocean carbon inventories have evolved over time or how the storage has varied geographically over different time periods.

In 2003, the U.S. CLIVAR/CO₂ Repeat Hydrography Program began reoccupying a subset of the WOCE/JGOFS ocean survey lines. The program has identified 19 hydrographic sections distributed around the global ocean that will be reoccupied approximately every 10 years to examine changes in ocean carbon and other physical and biogeochemical tracers (<http://ushydro.ucsd.edu/>). This work is being conducted in collaboration with other nations that have similar repeat hydrography programs.

In 2009 a zonal line (designated as I5) across the southern Indian Ocean, nominally along 32°S, was completed as part of the U.S. CLIVAR/CO₂ Repeat Hydrography Program. The top panel of Fig. 3.29 shows a section of dissolved inorganic carbon (DIC) along I5 in 2009. Unfortunately, very few DIC measurements were made on the previous occupation of I5 by the British in 2002, but DIC can be calculated with reasonable accuracy from the total alkalinity and spectrophotometric pH measurements that were made. The calculated 2002 DIC distributions are shown in the middle panel of Fig. 3.29. The accuracy of the calculated DIC values is estimated to be ±4

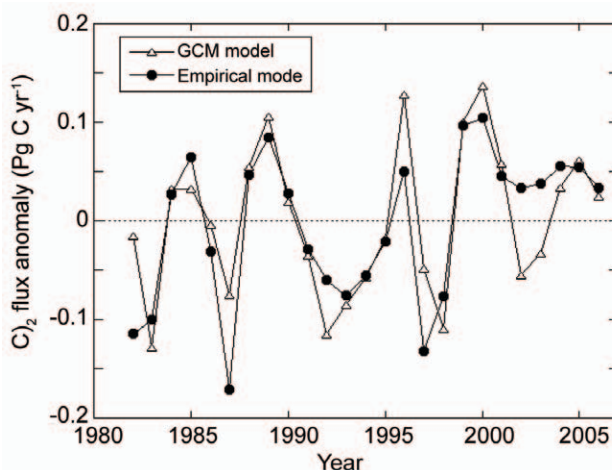


FIG. 3.28. Comparison of air-sea CO₂ flux anomalies in the Equatorial Pacific (10°S–10°N, 135°E–280°E) between the global ocean Community Climate System Model and the empirical model. Adapted from Park et al. (2010, manuscript submitted to *Tellus B*).

$\mu\text{mol kg}^{-1}$ or about half of the accuracy of the directly measured values. This accuracy was confirmed by comparison with a few dozen DIC samples that were collected and analyzed from the cruise.

To the first order the DIC distributions look similar for both years, but the difference plot (Fig. 3.29, bottom) shows that DIC generally increased throughout the upper 1000 m of the water column presumably resulting primarily from the uptake of anthropogenic CO_2 from the atmosphere. The magnitude of the changes is quite patchy with variations ranging from ~ -30 to $+30 \mu\text{mol kg}^{-1}$. These changes reflect natural carbon variations as well as secular anthropogenic carbon increases.

A full global assessment of ocean DIC changes cannot be made until the resurvey of the oceans is completed in the next few years. However, a promising new approach for estimating C_{ant} accumulation in

the ocean was recently published by Khatiwala et al. (2009). Their approach is based on an inverse method to estimate the ocean's transport from observed tracer distributions together with an estimate of the spatiotemporally varying air-sea CO_2 disequilibrium based on the long-term record of atmospheric CO_2 concentrations. The latter, which is also constrained by surface ocean pCO_2 data (Takahashi et al. 2009b), provides a time-varying boundary condition that can be used to compute the C_{ant} at any point in the ocean at any instant in time using the transport estimate. Khatiwala et al. have used this technique to reconstruct the spatially-resolved, time-dependent history of C_{ant} and its air-sea flux between 1765 and 2008. By taking into account the changing air-sea disequilibrium of CO_2 and the complex advective-diffusive transport of tracers in the ocean, this approach overcomes some of the main limitations and

biases of previous techniques. However, it does not account for potential changes in the fundamental processes controlling the distribution of natural carbon in the ocean such as variations in large-scale circulation, ventilation, or in the biological carbon pump.

Figure 3.30 shows a map of the C_{ant} column inventory in 2008 estimated using the method of Khatiwala et al. (2009). The first order patterns are very similar to those determined from the independent approach of Sabine et al. (2004) with the largest inventories in the North Atlantic, where the formation of deep waters move C_{ant} into the ocean interior. Relatively large inventories are also associated with the subtropical convergence zone at approximately 40°S in the Southern Hemisphere. The total 2008 inventory estimated for the mapped region in Fig. 3.30 is 140 Pg C. Adding in the Arctic Ocean inventory as estimated by Tanhua et al. (2009) and the marginal seas using the same scaling function as Sabine et al. (2004) gives a total global ocean inventory of 151 Pg C. This estimate suggests a 33 Pg C increase in inventory since the Sabine et al. estimate for 1994 reflecting the continued uptake and storage of C_{ant} at rates of 2.0 and $2.3 \pm 0.6 \text{ Pg C yr}^{-1}$ for the decades of the 1990s and 2000s, respectively (Khatiwala et al. 2009).

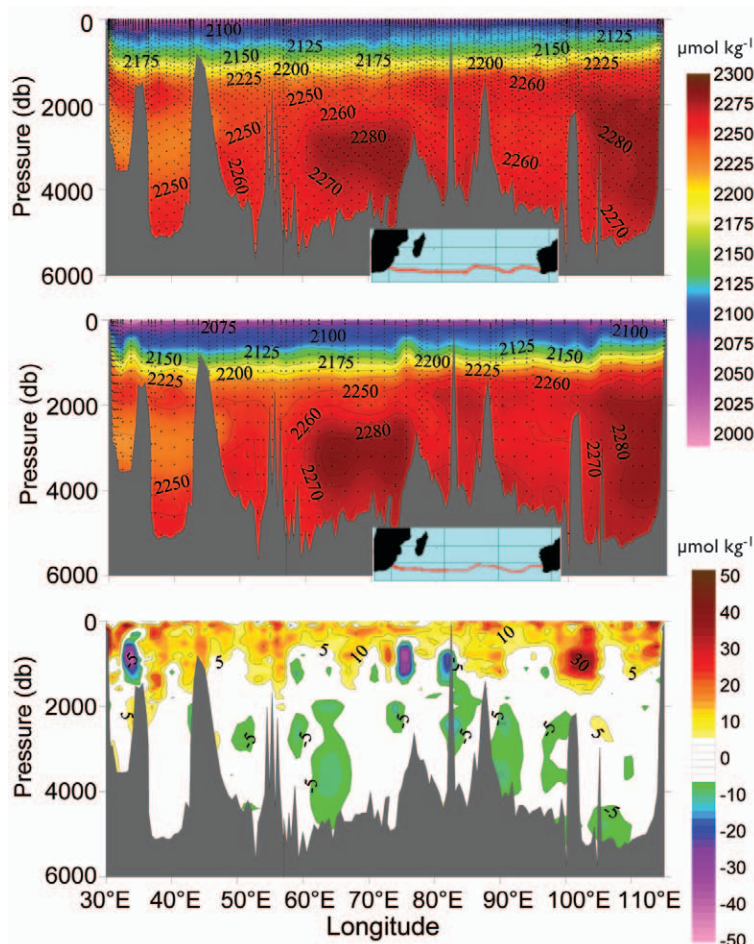


FIG. 3.29 Sections of dissolved inorganic carbon ($\mu\text{mol kg}^{-1}$) nominal along 32°S in 2009 (top) and 2002 (middle). The 2002 DIC values were calculated from total alkalinity and pH measurements (see text). Black dots show sample locations. Inset map shows cruise track in red. The bottom section shows the DIC change ($\mu\text{mol kg}^{-1}$) between the two cruises (2009 minus 2002).

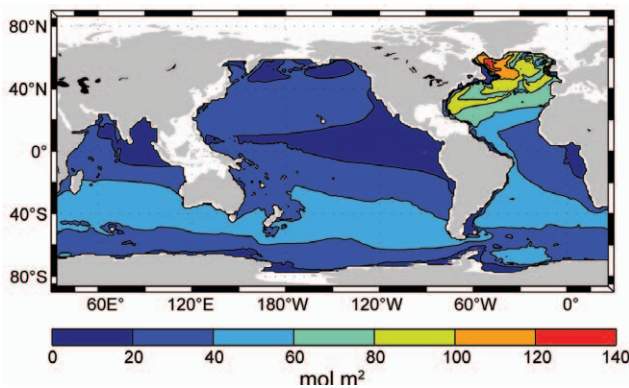


FIG. 3.30. Map of the column inventory of anthropogenic CO₂ in 2008. Adapted from Khatiwala et al. 2009.

One advantage of the Khatiwala estimates is the ability to examine the changes in ocean carbon storage over time. For example, these estimates suggest that the annual rate of ocean carbon storage has grown every year since the late 1700s, but the rate increased sharply in the 1950s in response to faster growth in atmospheric CO₂. In recent decades, however, the rate of increase in ocean carbon storage has not been able to keep pace with the atmospheric growth rate. The percentage of annual anthropogenic CO₂ emissions stored in the ocean in 2008 was as much as 10% smaller than the percentages of the previous decade, although significant uncertainties remain which preclude a more definitive statement. The rapid growth in emissions over the past 10 years relative to the previous decade is one important factor in the reduction in the ocean's relative uptake of anthropogenic CO₂ emissions. Another key factor is the decreasing ability of the seawater to store the CO₂ as dissolved inorganic carbon. This reduced capacity is a natural and predictable consequence of ocean carbon chemistry that, in the absence of changes in large-scale circulation or ocean biology, will become more significant with time (Eggleston et al. 2010). By comparing the Khatiwala estimates at the time and location of the repeat hydrography cruises the measured ocean carbon changes can be used to validate the C_{ant} estimates and monitor for changes in the natural ocean carbon cycle not constrained by the Khatiwala technique.

j. Global ocean phytoplankton—R. T. O'Malley, M. J. Behrenfeld, D. A. Siegel, and S. Maritorena

Photosynthesis by the free-floating, single-celled phytoplankton of the upper-sunlit "photic" layer of the global ocean is the overwhelmingly dominant source of organic matter fueling marine ecosystems. Phytoplankton contribute roughly half of the annual

biospheric (i.e., terrestrial and aquatic) net primary production (NPP; gross photosynthesis minus plant respiration), and their photosynthetic carbon fixation is the primary conduit through which atmospheric CO₂ is transferred into the ocean's organic carbon pools. These tiny suspended ocean "plants" play a vital role on the Earth's biogeochemical cycles, and are the very base of the oceanic food chain. The productivity of phytoplankton depends on the availability of sunlight, macronutrients (e.g., nitrogen, phosphorous), and micronutrients (e.g., iron), and thus is sensitive to changes in these resources.

Since 1997, a continuous record of global satellite ocean color observations has been available, allowing the investigation of relationships between ocean environmental conditions and plankton ecology (e.g., McClain 2009; Behrenfeld 2010). The ecosystem property most often derived from ocean color data is surface chlorophyll concentration (Chl_{sat}) (Fig. 3.31a). Chl_{sat} provides an estimate of phytoplankton pigment concentration throughout the upper ocean mixed layer and its variability reflects the combined influence of phytoplankton standing stock (biomass) changes and physiological responses to prevailing light and nutrient levels. Values of Chl_{sat} span three orders of magnitude globally (roughly 0.03 to $>30 \text{ mg m}^{-3}$) with a distribution closely aligned with primary ocean circulation features. Thus, high Chl_{sat} is found in regions of seasonal deep mixing (e.g., North Atlantic) and upwelling (e.g., Equatorial Pacific, west coast of Africa), while low values are found in permanently stratified ocean regions, particularly the low-nutrient central ocean gyres (white contours in Fig. 3.31a).

Climate-scale analyses require both *continuity* and *consistency* in the underlying observations for correct assessments of change. Unfortunately, these attributes are not satisfied for the most recent period of satellite ocean color measurements. Starting in 2008 and after more than a decade of continuous coverage, observations from the Sea-viewing Wide-Field-of-view Sensor (SeaWiFS) became intermittent due to issues with the spacecraft and telemetry. No SeaWiFS imagery was collected for the first 88 days of 2008 and, over the whole year, only 31 of 46 possible eight-day composite images could be processed. Data gaps also exist for 2009, with only 34 valid eight-day composites available over the year. Thus, 30% of the SeaWiFS record is missing for 2008/09 and only one-third of the eight-day composites are temporally matched for the two years. This lack of continuity strongly restricts an interannual comparison. Fortunately, half of the

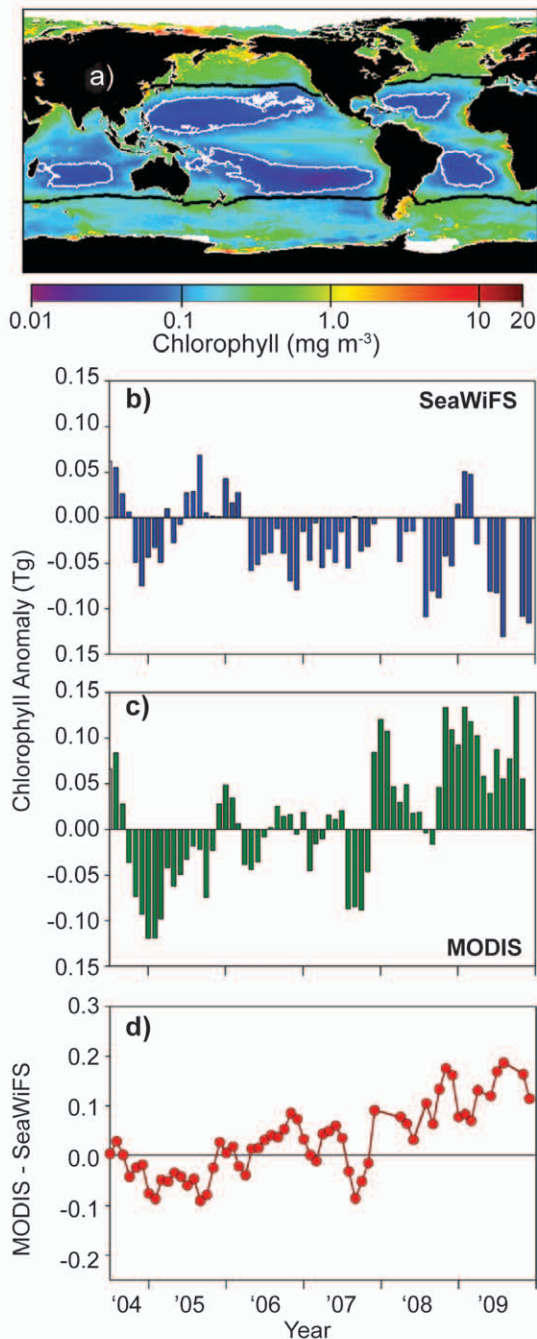


FIG. 3.31. (a) Average MODIS-Aqua Chl_{sat} for 2009. Heavy black lines indicate where average SST = 15°C, which is used herein to distinguish the permanently stratified ocean from northern and southern strongly-seasonal regions. White contours identify central ocean gyres, as defined by average Chl_{sat} values of 0.07 mg m^{-3} (see also McClain et al. 2004; Polovina et al. 2008; and Henson et al. 2009). (b) Mid-2004 through 2009 monthly chlorophyll anomalies for the SeaWiFS (data from latest reprocessing: r2009.1). (c) Mid-2004 through 2009 monthly chlorophyll anomalies for the MODIS-Aqua. (d) MODIS-SeaWiFS anomaly difference. Data in (b), (c), and (d) are for the permanently stratified oceans (average SST > 15°C).

coverage common to both years occurred at the end of the calendar year, providing two months of continuous coverage of the El Niño event developing over the latter half of 2009 (Chapter 4a).

Consistency between available U.S. ocean color datasets is also a problem. In the *State of Climate in 2008* report, we noted a relatively constant offset between the SeaWiFS Chl_{sat} record and concurrent data from the MODerate resolution Imaging Spectrometer (MODIS) on the *Aqua* platform. Accordingly, we found reasonable agreement between temporal chlorophyll anomalies for the two sensors (Behrenfeld et al. 2009) [as in the current report, anomalies were calculated as the difference between an observed value for a given month and the average value for that month over a sensor's full record (e.g., 1997–2009 for the SeaWiFS)]. Unfortunately, discrepancies between Chl_{sat} anomalies for the SeaWiFS (Fig. 3.31b) and MODIS-Aqua (Fig. 3.31c) increased during 2009, such that a simple offset correction is no longer adequate. The temporal evolution of this intersensor inconsistency is clearly revealed in the MODIS-SeaWiFS anomaly difference for the period 2004 to 2009 (Fig. 3.31d). While this issue of inconsistency has limited the current analysis of Chl_{sat} changes to SeaWiFS data only, it is important to note that the full MODIS-Aqua dataset is currently being reprocessed by the NASA Ocean Biology Processing Group and preliminary comparisons between the SeaWiFS and reprocessed MODIS-Aqua scenes look excellent (see <http://oceancolor.gsfc.nasa.gov/REPROCESSING/R2009/> for more details). Nevertheless, this experience emphasizes the critical importance of monitoring and updating ocean color sensor calibrations/algorithms and conducting periodic data reprocessing to achieve data quality levels adequate for satellite-based global climate studies.

To investigate changes in global ocean chlorophyll stocks during 2009, available SeaWiFS data were analyzed following methodologies originally described in Behrenfeld et al. (2006) and employed in our two previous *State of the Climate* reports (Behrenfeld et al. 2008b, 2009). Chl_{sat} data (mg m^{-3}) were integrated to the 1% light level to calculate "photic zone" chlorophyll concentrations (ΣChl). For analysis of chlorophyll anomaly trends, global data were binned into three broad regions: the permanently stratified ocean (approximated as those waters with annual average SST > 15°C), strongly seasonal high-latitude northern waters (average SST < 15°C), and strongly-seasonal high-latitude southern waters (average SST < 15°C).

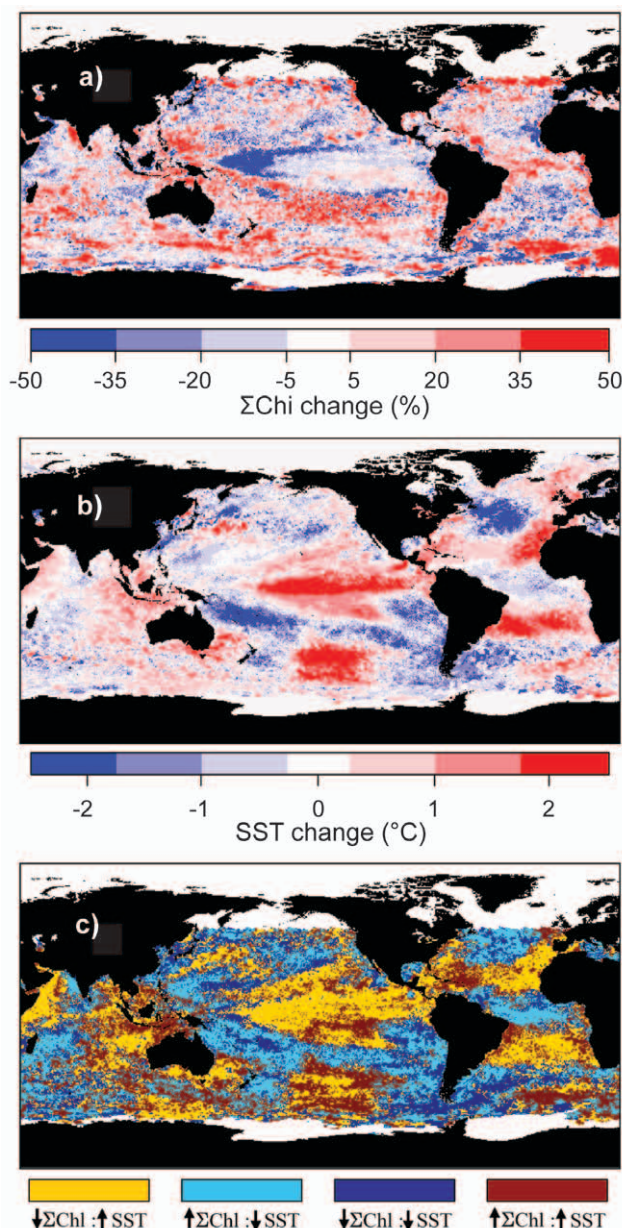


FIG. 3.32. (a) Percent change in November–December average depth-integrated chlorophyll (ΣChl) between 2009 and 2008. (b) Absolute change in November–December average SST between 2009 and 2008. (c) State-space comparison between ΣChl and SST (from panels a and b). Yellow = increasing SST, decreasing ΣChl . Red = increasing SST, increasing ΣChl . Dark blue = decreasing SST, decreasing ΣChl . Light blue = decreasing SST, increasing ΣChl .

For each region, ΣChl data (mg m^{-2}) were summed over surface area to give total chlorophyll stocks in units of teragrams ($\text{Tg} = 10^{12} \text{ g}$).

Spatiotemporal variations in Chl_{sat} are driven by variability in phytoplankton biomass, nutrient stress, and light acclimation (i.e., photoacclimation),

all of which are linked to physical changes within the surface mixed layer. Changes in SST provide one index of this variability in the physical environment and can be compared globally to changes in Chl_{sat} (Behrenfeld et al. 2006, 2008a, 2009). The relationship between phytoplankton chlorophyll and SST changes for the 2008 to 2009 period is best illustrated over the November–December period corresponding to the strengthening of the 2009 El Niño (Fig. 3.32). For this period, expansive and spatially coherent regions are seen of increasing and decreasing ΣChl (Fig. 3.32a). In particular, ΣChl decreased over much of the equatorial Pacific in response to lower nutrient levels associated with reduced rates of upwelling. In contrast, significant increases in ΣChl are found in the western tropical Pacific, the south Pacific and Indian subtropical gyres and the equatorial Atlantic Ocean (Fig. 3.32a). These changes in ΣChl correspond to similar spatial patterns in SST changes (Fig. 3.32b), again illustrating the close link between ocean biology and their physical environment.

Overall for the stratified oceans, 63% of the pixels with increased SST for November–December 2009 also exhibited decreased in ΣChl (yellow pixels in Fig. 3.32c). Likewise, 60% of the pixels with decreased SST corresponded to increased ΣChl (light blue pixels in Fig. 3.32c). This dominant inverse relationship between SST changes and ΣChl changes is consistent with surface-ocean warming (cooling) being associated with decreasing (increasing) vertical nutrient transport and increasing (decreasing) mixed-layer light levels, with light and nutrient changes driving changes in both phytoplankton cellular pigment levels and biomass.

Relationships between global chlorophyll fields and SST illustrated in Fig. 3.32 are seen at a much broader level when cast against the full 12-year SeaWiFS record for the three regions described above. For this comparison, monthly anomalies in regional SeaWiFS chlorophyll stocks were matched to SST anomalies constructed by merging MODIS-*Aqua* SST4 data (2003–09) and AVHRR (quality 5–8) SST data (1997–2003) (regionally-integrated SST data have units of $^{\circ}\text{C m}^2$ and are hereafter referred to as "thermal anomalies"). Once again, an overall inverse relationship emerges at the regional scale for the full SeaWiFS record [Fig. 3.33 – note that the thermal anomaly axes are inverted (i.e., cooling at top, warming at bottom)]. Indeed, the newly reprocessed SeaWiFS data provides an even closer match between thermal anomalies and chlorophyll anomalies than previously reported (e.g., compare to Behrenfeld et al. 2009). At high-northern

latitudes, chlorophyll and thermal oscillations were relatively constrained between 1997 and 2006 and then showed significantly stronger variability (Fig. 3.33a). As in previous reports (Behrenfeld et al. 2008b, 2009), chlorophyll and thermal anomalies exhibited

the largest temporal changes in the permanently stratified, lower-latitude oceans (Fig. 3.33b – note different axis scaling), with a large initial trend of increasing chlorophyll and decreasing temperature associated with the 1997–99 El Niño (Behrenfeld et al. 2006). From 1999 onward, an overall progressive decrease in chlorophyll is observed and coincident with a general increasing trend in ocean-surface temperature (Fig. 3.33b). At high southern latitudes, temporal trends in chlorophyll and thermal anomalies are weaker (Fig. 3.33c).

While comparisons of surface chlorophyll and temperature data illustrate the strong dependencies of biology on physical forcings, it is important to recognize that the underpinnings of such relationships are correlative not causative. For each region, the full range in thermal anomalies represents an average change in SST that barely spans 1°C. The direct physiological consequences (e.g., enzymatic reaction rates) of such minute temperature changes are negligible. Thus, correlations between SST and chlorophyll anomalies emerge because SST acts as a surrogate for other environmental factors that covary with SST and directly impact phytoplankton chlorophyll levels. Two such factors are nutrient supply and mixed-layer light levels. In general, surface-layer warming is associated with stronger surface-layer stratification and shallower mixing depths, which in turn increase average mixed-layer phytoplankton light exposure and can hamper vertical nutrient exchange (Behrenfeld et al. 2005; Siegel et al. 2005). Decreased nutrient availability suppresses phytoplankton cellular chlorophyll levels and can diminish phytoplankton biomass. Likewise, acclimation to enhanced mixed-layer light exposure entails reductions in cellular chlorophyll. Changes in seasonal surface mixing cycles can also influence chlorophyll levels by altering predator–prey interactions and thereby phytoplankton biomass and species composition (Behrenfeld 2010). Thus, it is the correlation between SST and the summed expression of these, and other, direct forcings that gives rise to inverse chlorophyll–SST relationships. It is essential that these *functional* relationships be carefully considered when interpreting observed global changes in satellite chlorophyll fields and when projecting observed changes to longer time-scale trends.

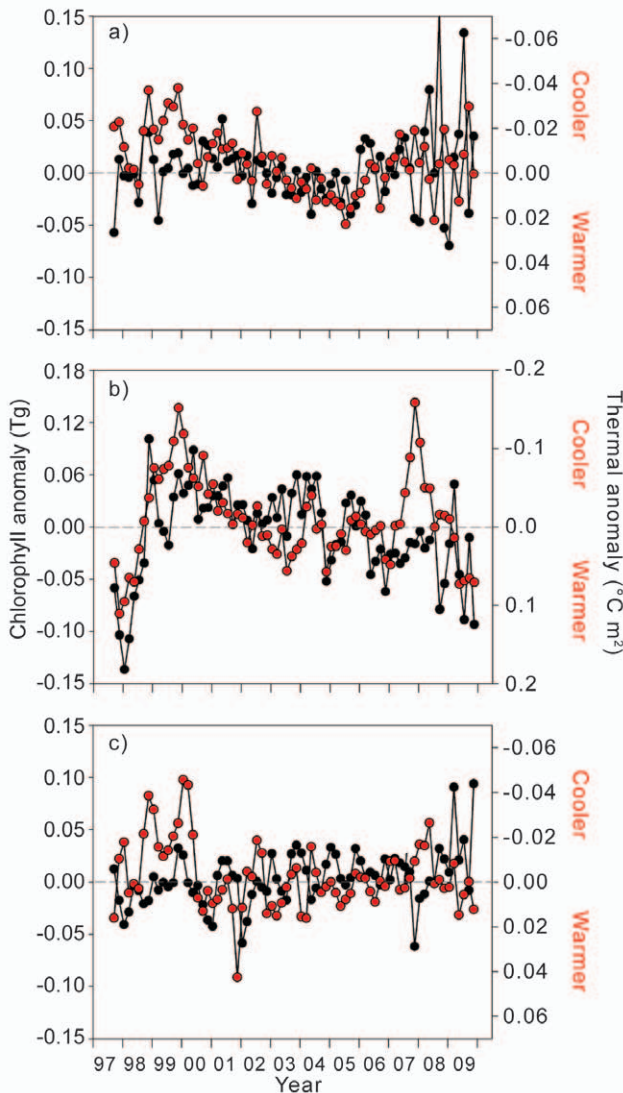


FIG. 3.33. Twelve-year record of monthly SeaWiFS chlorophyll anomalies (black symbols, left axis, Tg) and monthly AVHRR/MODIS thermal anomalies (red symbols, right axis, °C m² x 10¹⁵). (a) Northern waters with average SST < 15°C. (b) Permanently stratified waters with average SST > 15°C. (c) Southern waters with average SST < 15°C. See Fig. 3.31a for location of each region. Horizontal dashed line in each panel = 0. Thermal anomaly axes (right) are inverted to illustrate the general inverse relationship with chlorophyll anomalies and thermal anomalies. Note that the use of thermal anomalies in this figure differs from Behrenfeld et al. 2008b and 2009. This change was made to preserve identical processing with the chlorophyll signal.